

Gigaelectronvolt emission from a compact binary merger

<https://doi.org/10.1038/s41586-022-05404-7>

Received: 17 May 2022

Accepted: 3 October 2022

Published online: 7 December 2022

 Check for updates

Alessio Mei^{1,2}✉, Biswajit Banerjee^{1,2}, Gor Oganesyan^{1,2}, Om Sharan Salafia^{3,4,5}, Stefano Giarratana^{6,7}, Marica Branchesi^{1,2}, Paolo D'Avanzo⁵, Sergio Campana⁵, Giancarlo Ghirlanda^{4,5}, Samuele Ronchini^{1,2}, Amit Shukla⁸ & Pawan Tiwari⁹

An energetic γ-ray burst (GRB), GRB 211211A, was observed on 11 December 2021^{1,2}. Despite its long duration, typically associated with bursts produced by the collapse of massive stars, the observation of an optical-infrared kilonova points to a compact binary merger origin³. Here we report observations of a significant (more than five sigma) transient-like emission in the high-energy γ-rays of GRB 211211A (more than 0.1 gigaelectronvolts) starting 10^3 seconds after the burst. After an initial phase with a roughly constant flux (about 5×10^{-10} erg per second per square centimetre) lasting about 2×10^4 seconds, the flux started decreasing and soon went undetected. Our detailed modelling of public and dedicated multi-wavelength observations demonstrates that gigaelectronvolt emission from GRB 211211A is in excess with respect to the flux predicted by the state-of-the-art afterglow model at such late time. We explore the possibility that the gigaelectronvolt excess is inverse Compton emission owing to the interaction of a late-time, low-power jet with an external source of photons, and find that kilonova emission can provide the seed photons. Our results open perspectives for observing binary neutron star mergers.

Gamma (γ)-ray bursts (GRBs) are extragalactic transients that release an enormous amount of (isotropic equivalent) energy, of the order of $10^{52}\text{--}10^{54}$ erg. The initial highly variable γ-ray radiation (called ‘prompt emission’) is a short-lived burst ($0.1\text{--}10^3$ s) in the γ-ray band (10 keV–10 MeV) originating from internal dissipation of energy within an ultra-relativistic jet^{4–6}. The propagation of the GRB jet into the circum-burst medium produces a shock wave that gives rise to a multi-wavelength, longer-lived afterglow emission owing to synchrotron radiation from non-thermal electrons^{7,8}. GRBs are classified into two classes on the basis of the duration of their prompt emission: ‘long’ (LGRBs, longer than 2 s) and ‘short’ (sGRBs, shorter than 2 s)⁹. Over recent decades, extensive GRB studies have demonstrated that their spectral properties, afterglow emission and host galaxies are consistent with two types of progenitor¹⁰. Although a number of supernovae of the Ib/c class detected in association with LGRBs¹¹ have revealed massive star collapse progenitors, the sGRB GRB 170817A detected in close temporal association with the gravitational wave (GW) signal GW170817^{12–14} showed that binary neutron star (BNS) mergers are the progenitors of sGRBs. A key feature of compact object mergers involving at least one neutron star is the kilonova, an optical-infrared transient powered by radioactive decay of unstable heavy isotopes synthesized by rapid neutron capture by nuclei within the expanding neutron-rich merger ejecta^{15,16}. Signatures of the presence of such an emission have been observed following several sGRBs^{17–22}, and the first spectroscopic confirmation and detailed multi-wavelength characterization came with the AT2017gfo kilonova after GW170817^{13,23–25}.

On 11 December 2021 at 13:09:59 Universal Time (UT) a burst triggered the Burst Alert Telescope (BAT) onboard the Swift satellite¹ and the Gamma-ray Burst Monitor (GBM) onboard the Fermi satellite². The GRB 211211A showed duration and properties typical of LGRBs, but right after its detection, several outstanding features came into sight. Deep optical observations revealed that this source is strongly offset with respect to the centre of its host galaxy, placed at redshift $z = 0.076$ (350 Mpc)³. A kilonova emission was discovered in the optical/near-infrared (NIR) band in temporal and spatial coincidence with the burst³. In addition, the γ-ray precursor anticipating the prompt emission shows signatures of quasi-periodic oscillations²⁶. Despite its long duration as estimated by Swift and Fermi, these interesting discoveries are pointing towards a compact binary merger progenitor, strongly challenging the above sGRB and LGRB progenitor dichotomy and opening a door to a more complex classification scheme for GRBs.

Here we report another discovery for the GRB 211211A; the detection, in the Fermi Large Area Telescope (LAT) data, of a significant ($>5\sigma$) emission with photon energies between 0.1 GeV and 1 GeV (Fig. 1). The emission showed up significantly ($\geq 3\sigma$) about 6 ks after the burst and remained constant for about other 14 ks. It is characterized by a relatively soft spectrum with power-law photon index of 2.9 ± 0.4 . We measure a flux of $(5.21 \pm 1.52) \times 10^{-10}$ erg s⁻¹ cm⁻² between 0.1 GeV and 1 GeV (integrated between 1 ks and 20 ks after the trigger time) which, given the source distance, corresponds to a luminosity of $(7.4 \pm 2.2) \times 10^{45}$ erg s⁻¹, which is particularly low compared with the GRBs observed so far at similar times and frequencies by Fermi/LAT²⁷, as shown in Fig. 2. This intrinsically faint emission would be hardly

¹Gran Sasso Science Institute, L’Aquila, Italy. ²INFN - Laboratori Nazionali del Gran Sasso, L’Aquila, Italy. ³Università degli Studi di Milano-Bicocca, Milan, Italy. ⁴INFN - Sezione di Milano-Bicocca, Milan, Italy. ⁵INAF - Osservatorio Astronomico di Brera, Merate, Italy. ⁶INAF - Istituto di Radioastronomia, Bologna, Italy. ⁷Department of Physics and Astronomy, University of Bologna, Bologna, Italy. ⁸Department of Astronomy, Astrophysics and Space Engineering, Indian Institute of Technology Indore, Indore, India. [✉]e-mail: alessio.mei@gssi.it

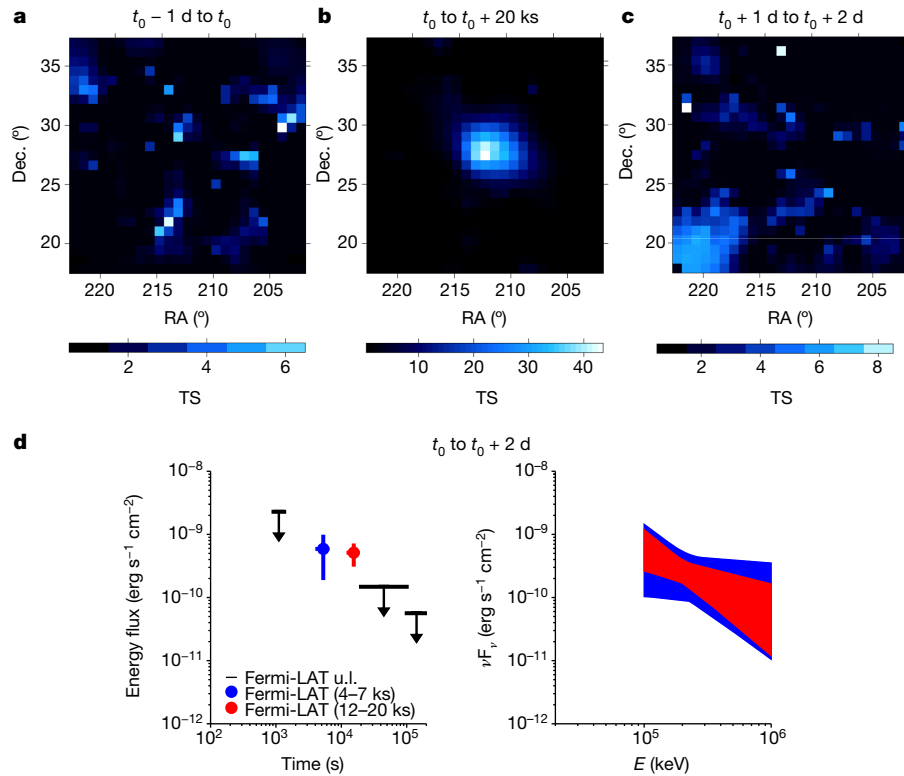


Fig. 1 | Fermi/LAT detection of GRB 211211A. **a–d**, TS maps (**a–c**) centred at the GRB position ($\text{RA} = 212.272^\circ$, $\text{Dec.} = 27.884^\circ$) and the GRB light curve and spectrum (**d**). With respect to the GRB 211211A trigger time t_0 , the TS maps are shown: one day before t_0 (**a**), during the first 6 h after t_0 (**b**) and one day after t_0 (**c**). Although a significant excess has been observed within 1–20 ks after the GRB

trigger time reaching a TS of about 43, no significant excess has been observed in any other time bins. **d**, Left: the GRB 211211A light curve between 0.1 GeV and 1 GeV. Flux upper limits are shown (in black) for the epochs with $\text{TS} < 9$. Right: the two spectra are between 4–7 ks (blue) and 12–20 ks (red). We report error bars and upper limits (u.l.) with 1σ and 2σ confidence levels, respectively.

detected at distances larger than 350 Mpc. Such a late-time emission in the Fermi/LAT data is not present in any other GRBs closer than 350 Mpc (Methods), and it has not been reported for sGRBs at any distances (Fig. 2). For GW170817, no Fermi/LAT detection was reported on timescales of minutes, hours and days after the BNS merger²⁸, making the gigaelectronvolt emission of GRB 211211A a high-energy component

observed in association with a compact binary merger event (Methods). Recently, gigaelectronvolt emission has been detected from a binary system containing one massive star and one compact object²⁹.

We have followed up GRB 211211A with the High Throughput X-ray Spectroscopy Mission (XMM-Newton) in soft X-rays (0.3–10 keV) 9.6 d and 51 d after the GRB trigger time and we have obtained deep upper

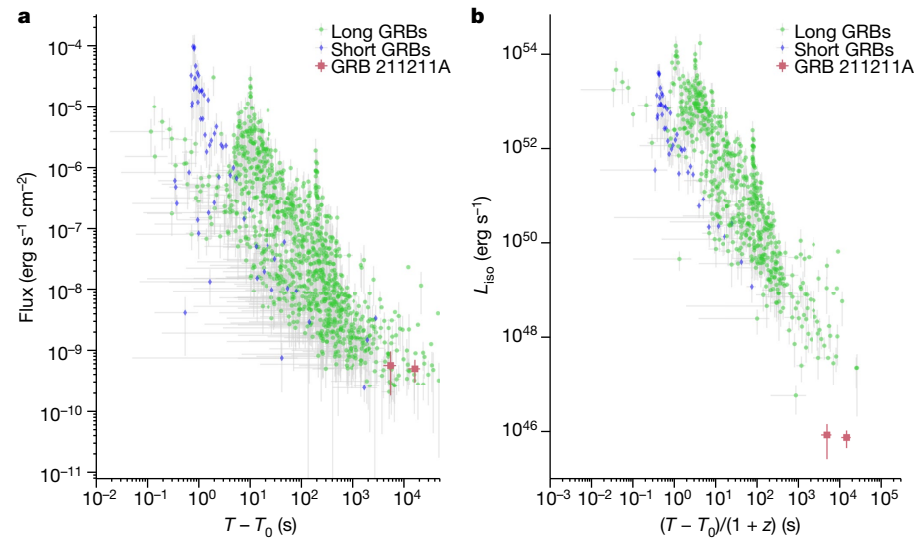


Fig. 2 | High-energy light curves of GRBs observed by Fermi/LAT. Long (green) and short (blue) LAT light curves from the second Fermi/LAT GRB catalogue²⁷ compared with GRB 211211A emission (brown). **a**, The LAT flux in the energy band of 0.1–10 GeV as a function of time from the burst trigger time T_0

obtained through time-resolved analysis with a test statistic $\text{TS} > 9$. **b**, For the sub-sample of IGRBs and sGRBs with redshift estimates (about 34 sources), we show the isotropic-equivalent LAT luminosity L_{iso} as a function of the rest-frame time after trigger. Error bars are reported with 1σ confidence level.

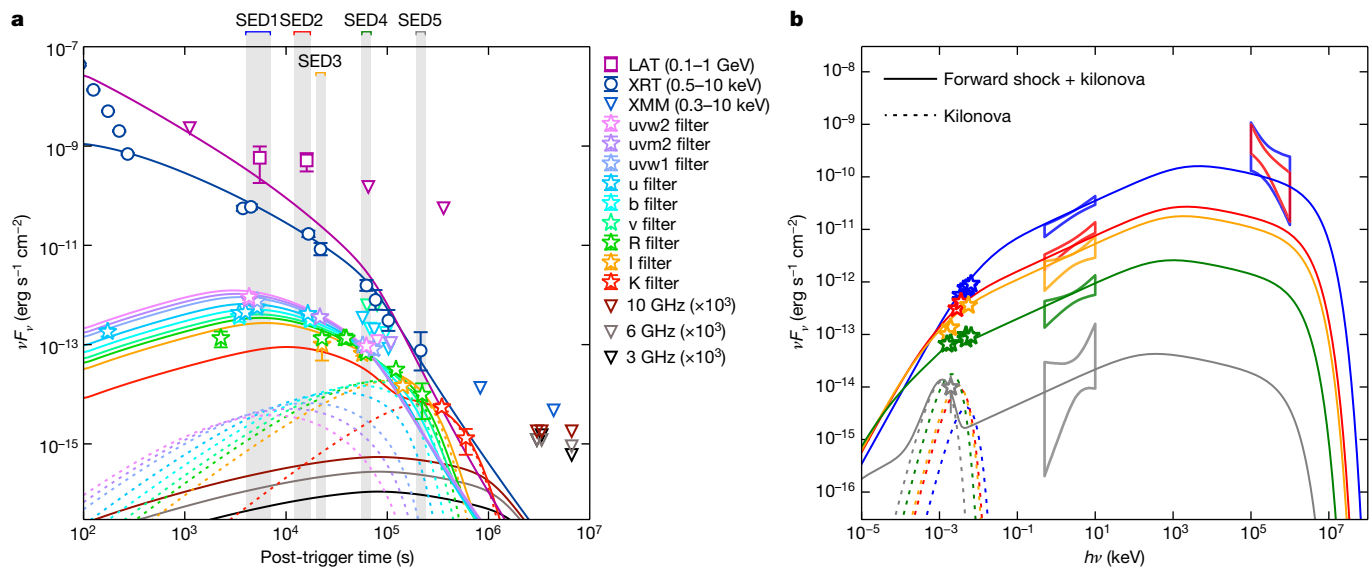


Fig. 3 | Multi-wavelength light curves and spectra of GRB 211211A. **a,b,** Light curves (**a**) and SEDs (**b**) of GRB 211211A. Fluxes inferred from observations are shown by circles, squares or stars with 1σ error bars, and downward-pointing triangles indicate 3σ upper limits (multiplied by 10^3 in the case of radio observations). In **b**, butterfly-shaped symbols show 1σ flux confidence regions for Swift/XRT and Fermi/LAT. The solid lines show our best-fitting model, consisting of emission from the forward shock and a kilonova. The model radio light curves are multiplied by 10^3 , consistent with the corresponding datapoints. The dotted lines single out the kilonova contribution. The SEDs are relative to the time bins marked with vertical grey bands in **a**.

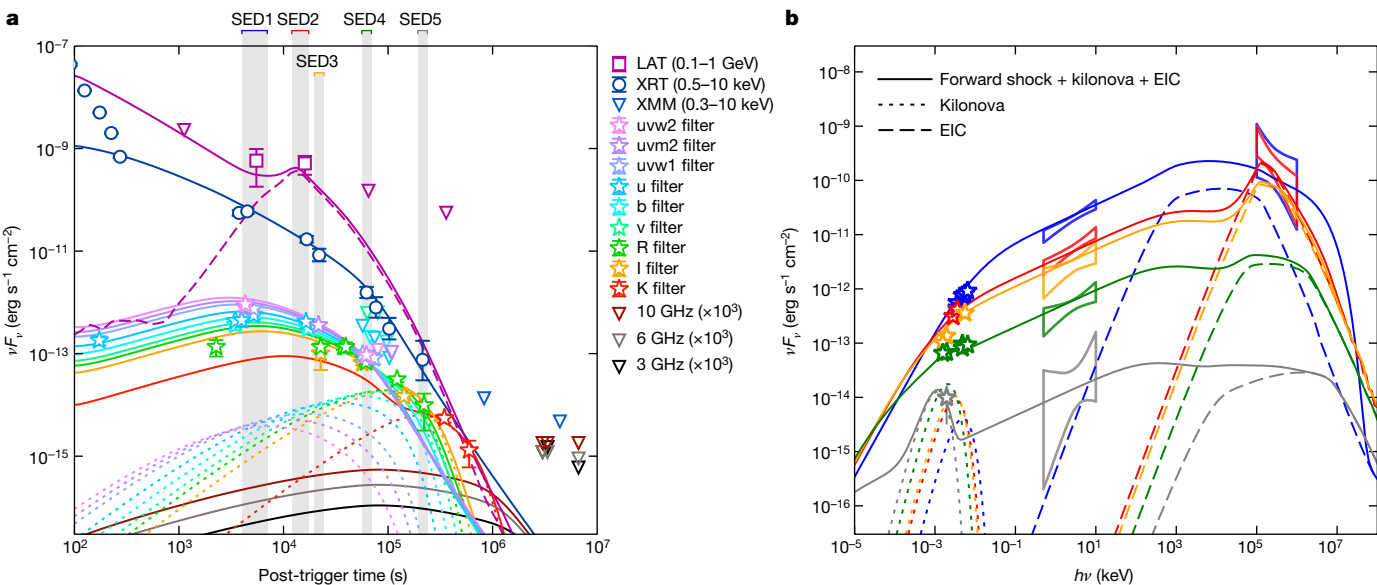
for Swift/XRT and Fermi/LAT. The solid lines show our best-fitting model, consisting of emission from the forward shock and a kilonova. The model radio light curves are multiplied by 10^3 , consistent with the corresponding datapoints. The dotted lines single out the kilonova contribution. The SEDs are relative to the time bins marked with vertical grey bands in **a**.

limits of 10^{-14} erg s $^{-1}$ cm $^{-2}$ and 5×10^{-15} erg s $^{-1}$ cm $^{-2}$, respectively. A search for late radio afterglow emission was performed 35 d, 39 d and 77 d post-burst with the Karl G. Jansky Very Large Array (VLA) at frequencies of 3 GHz, 6 GHz and 10 GHz. We did not detect any emission also at these frequencies. To fully characterize the afterglow emission of this source, we enriched our dataset with publicly available data from Swift X-ray Telescope (XRT), Swift Ultra-violet Optical Telescope (UVOT), and photometry from ground-based optical and infrared telescopes (see Methods for details). We model radio-to-gigaelectronvolt observations within the standard afterglow scenario⁶, including synchrotron and synchrotron self-Compton (SSC) radiation from shock-accelerated circum-burst medium electrons. We also include a simple one-component model for the kilonova emission (Methods). The model fit is in good agreement with the optical and X-ray light

curves, including the well constrained spectral shape of the soft X-ray emission and the very late epoch upper limits obtained with the VLA and XMM-Newton (Fig. 3).

The best-fit parameters of the afterglow suggest that the GRB jet is highly collimated (aperture angle $\theta_j \approx 1.0^{+0.5}_{-0.3}$ deg, 90% credible level) and it propagates in a rarefied circum-burst medium with a homogeneous number density $n \leq 8 \times 10^{-5}$ cm $^{-3}$ (95% credible upper limit), in agreement with what would be expected given the offset between this GRB and its host galaxy centre. The jet's total kinetic energy (corrected for collimation) $E_{\text{jet}} = 1.0^{+6.0}_{-0.9} \times 10^{50}$ erg is consistent with the amount of energy disposed in the jet formed from the BNS merger of GW170817 (for example, ref.³⁰).

Despite the good spectral and timing description of the optical and X-ray data by the combined standard afterglow and the kilonova



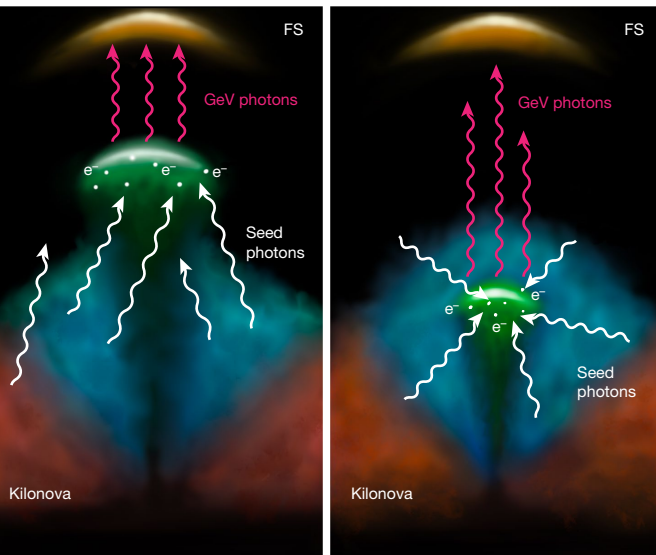


Fig. 5 | The interaction between the low-power jet and the kilonova.

a,b, Artistic impression of the scenario explaining the Fermi/LAT observations of the GRB 211211A. Seeds photons emitted from the kilonova ejecta (red and blue) are scattered via inverse Compton by electrons in a low-power jet (green) launched at late times. The EIC can occur at a radius above (a) or below (b) the kilonova surface. The external forward shock of the relativistic jet giving rise to multi-wavelength afterglow emission is shown in yellow.

models, the high-energy emission component at late times remains in excess with respect to the standard forward shock radiation. Although the first epoch of the Fermi/LAT observation (4–7 ks) is consistent with the synchrotron component of the forward shock, the second one (between 12 ks and 20 ks) is in clear excess over the expected power-law decay of the afterglow ($\propto t^{-1}$; where t is time; Fig. 3). Such a late excess could originate from the external inverse Compton (EIC) process, that is, from photons produced externally with respect to the GRB jet that are upscattered by electrons within the latter. A possible source of external photons is the kilonova emission. Its thermal emission spectrum, Comptonized by the jet electrons, would account for the relatively soft observed gigaelectronvolt spectrum and would not contaminate the soft X-ray, which is well described by the synchrotron emission. Assuming the kilonova photons to be the seed photons for the EIC, we conclude that the relativistic electrons from the forward shock responsible for the multi-wavelength emission cannot reproduce the observed luminosity of the gigaelectronvolt component. This is because at about 10^4 s, the dominant photons would come from the forward shock, but the SSC peaks at higher energies and its contribution is negligible to the gigaelectronvolt emission. However, a source of hot electrons closer to the kilonova ejecta can account for the EIC component. We invoke the presence of a low-power jet ejected at late times, whose electrons are capable of producing the amount of gigaelectronvolt emission without over-shining the overall multi-wavelength afterglow emission by the synchrotron radiation (see Fig. 4).

If the hot electrons are placed above the kilonova photosphere (de-beamed scenario, Fig. 5a) the EIC process is inefficient and it requires a very low magnetization of the jet to not outshine the observed afterglow emission by the synchrotron radiation. Instead, we show that a scenario where such electrons reside below the kilonova photosphere at $t = 10^4$ s (beamed scenario, Fig. 5b) leads to beamed seed photons in the comoving frame of the jet, hence explaining the observed gigaelectronvolt emission by inverse Compton scattering of the kilonova photons without extreme requirements on the magnetic field strength (see Methods for details). Gigaelectronvolt emission from upscattered kilonova photons opens perspectives for detecting

kilonova emission at high energies and it represents another relevant electromagnetic counterpart of gravitational waves from compact binary mergers.

Online content

Any methods, additional references, Nature Portfolio reporting summaries, source data, extended data, supplementary information, acknowledgements, peer review information; details of author contributions and competing interests; and statements of data and code availability are available at <https://doi.org/10.1038/s41586-022-05404-7>.

- D'Ai, A. et al. GRB 211211A: Swift detection of a bright burst. *GRB Coord. Netw. Circ.* No. 31202 (2021).
- Fermi GBM Team GRB 211211A: Fermi GBM final real-time localization. *GRB Coord. Netw. Circ.* No. 31201 (2021).
- Rastinejad, J. C. et al. A kilonova following a long-duration gamma-ray burst at 350 Mpc. *Nature* <https://doi.org/10.1038/s41586-022-05390-w> (2022).
- Narayan, R., Paczynski, B. & Piran, T. Gamma-ray bursts as the death throes of massive binary stars. *Astrophys. J.* **395**, L83 (1992).
- Rees, M. J. & Meszaros, P. Unsteady outflow models for cosmological gamma-ray bursts. *Astrophys. J.* **430**, L93 (1994).
- Sari, R., Narayan, R. & Piran, T. Cooling timescales and temporal structure of gamma-ray bursts. *Astrophys. J.* **473**, 204 (1996).
- Paczynski, B. & Rhoads, J. E. Radio transients from gamma-ray bursters. *Astrophys. J.* **418**, L5 (1993).
- Sari, R. & Piran, T. Predictions for the very early afterglow and the optical flash. *Astrophys. J.* **520**, 641–649 (1999).
- Kouveliotou, C. et al. Identification of two classes of gamma-ray bursts. *Astrophys. J.* **413**, L101 (1993).
- Berger, E. Short-duration gamma-ray bursts. *Annu. Rev. Astron. Astrophys.* **52**, 43–105 (2014).
- Woosley, S. E. & Bloom, J. S. The supernova gamma-ray burst connection. *Annu. Rev. Astron. Astrophys.* **44**, 507–556 (2006).
- Abbott, B. P. et al. GW170817: observation of gravitational waves from a binary neutron star inspiral. *Phys. Rev. Lett.* **119**, 161101 (2017).
- Abbott, B. P. et al. Multi-messenger observations of a binary neutron star merger. *Astrophys. J.* **848**, L12 (2017).
- Abbott, B. P. et al. Gravitational waves and gamma-rays from a binary neutron star merger: GW170817 and GRB 170817A. *Astrophys. J.* **848**, L13 (2017).
- Li, L.-X. & Paczynski, B. Transient events from neutron star mergers. *Astrophys. J.* **507**, L59–L62 (1998).
- Metzger, B. D. et al. Electromagnetic counterparts of compact object mergers powered by the radioactive decay of r-process nuclei. *Mon. Not. R. Astron. Soc.* **406**, 2650–2662 (2010).
- Tanvir, N. R. et al. A ‘kilonova’ associated with the short-duration γ-ray burst GRB 130603B. *Nature* **500**, 547–549 (2013).
- Berger, E., Fong, W. & Chornock, R. An r-process kilonova associated with the short-hard GRB 130603B. *Astrophys. J.* **774**, L23 (2013).
- Troja, E. et al. The afterglow and kilonova of the short GRB 160821B. *Mon. Not. R. Astron. Soc.* **489**, 2104–2116 (2019).
- Ascenzi, S. et al. A luminosity distribution for kilonovae based on short gamma-ray burst afterglows. *Mon. Not. R. Astron. Soc.* **486**, 672–690 (2019).
- Jin, Z.-P. et al. A kilonova associated with GRB 070809. *Nat. Astron.* **4**, 77–82 (2020).
- Rossi, A. et al. A comparison between short GRB afterglows and kilonova AT2017gfo: shedding light on kilonova properties. *Mon. Not. R. Astron. Soc.* **493**, 3379–3397 (2020).
- Pian, E. et al. Spectroscopic identification of r-process nucleosynthesis in a double neutron-star merger. *Nature* **551**, 67–70 (2017).
- Smartt, S. J. et al. A kilonova as the electromagnetic counterpart to a gravitational-wave source. *Nature* **551**, 75–79 (2017).
- Drout, M. R. et al. Light curves of the neutron star merger GW170817/SSS17a: implications for r-process nucleosynthesis. *Science* **358**, 1570–1574 (2017).
- Xiao, S. et al. The quasi-periodically oscillating precursor of a long gamma-ray burst from a binary neutron star merger. Preprint at <https://arxiv.org/abs/2205.02186> (2022).
- Ajello, M. et al. A decade of gamma-ray bursts observed by Fermi-LAT: the second GRB catalog. *Astrophys. J.* **878**, 52 (2019).
- Ajello, M. et al. Fermi-LAT observations of LIGO/Virgo event GW170817. *Astrophys. J.* **861**, 85 (2018).
- Xingling, H., Junpei, T. & Qingwen, T. GeV emission of gamma-ray binary with pulsar scenario. *Mon. Not. R. Astron. Soc.* **494**, 3699–3711 (2020).
- Salafia, O. S. & Giacomazzo, B. Accretion-to-jet energy conversion efficiency in GW170817. *Astron. Astrophys.* **645**, A93 (2021).

Publisher's note Springer Nature remains neutral with regard to jurisdictional claims in published maps and institutional affiliations.

Springer Nature or its licensor (e.g. a society or other partner) holds exclusive rights to this article under a publishing agreement with the author(s) or other rightsholder(s); author self-archiving of the accepted manuscript version of this article is solely governed by the terms of such publishing agreement and applicable law.

© The Author(s), under exclusive licence to Springer Nature Limited 2022

Article

Methods

Swift/XRT

We have downloaded the data provided by the XRT (0.3–10 keV) onboard the Neil Gehrels Swift Observatory (Swift) from the Swift Science Data Center supported by the University of Leicester³¹. Eight time bins (3.5–140 ks from the GRB trigger time) in the photon-counting mode were selected for the time-resolved spectral analysis to evaluate the temporal and spectral evolution of the X-ray emission during the afterglow phase. We have performed spectral analysis of XRT time-resolved spectra with XSPEC (v12.12.0) using the CSTAT likelihood. We have fitted the 0.3–10-keV spectra by a simple power law taking into account the Galactic absorption by applying the multiplicative ‘tbabs’ model. Galactic absorption by neutral hydrogen in the direction of the GRB is estimated from ref.³². We have additionally fitted all the time-resolved spectra by applying also the ‘tbabs’ model to account for the intrinsic absorption. We have found the intrinsic column density of the neutral hydrogen to be consistent with zero. Therefore, we have further excluded the intrinsic absorption from our modelling. The best-fit parameters, that is, unabsorbed flux and the photon index, were used for the modelling of the afterglow emission.

Swift/UVOT

The Swift/UVOT carried out observations of GRB 211211A between $T_0 + 92$ s and $T_0 + 3.3$ d, where T_0 is the trigger time. The GRB optical and ultraviolet afterglow was detected in all UVOT filters until $T_0 + 1.3$ d (refs.^{3,33}). We retrieved and analysed the Swift/UVOT data obtained with the white filter from the Swift archive (<https://heasarc.gsfc.nasa.gov/cgi-bin/W3Browse/swift.pl>). The afterglow magnitudes have been obtained with the task ‘uvotsource’, part of the HEASOFT software package (<https://heasarc.gsfc.nasa.gov/docs/software/heasoft/>), using a circular extraction aperture of 3” radius (to minimize contamination from the nearby host galaxy) and a background circular region of 20” radius. An aperture correction has been applied to report the obtained magnitudes to the standard 5” aperture. For the afterglow light curves in the other UVOT filters, we refer to the magnitudes values reported in ref.³.

Although we did not include, as a conservative choice, the white filter data in the model fitting, we estimated a posteriori its compatibility with our modelling as follows. Using the appropriate transmission curve (https://www.mssl.ucl.ac.uk/www_astro/uvot/uvot_instrument/), we found that, assuming a spectrum with an intrinsic power-law flux density $F_\nu \propto \nu^{-0.65}$ at a given frequency ν (corresponding to the spectral shape predicted by our model) and accounting for Galactic interstellar dust absorption with $E(B - V) = 0.015$ (ref.³⁴), the extinction-corrected white filter AB magnitude can be transformed into the equivalent u filter one by a +0.068 magnitude correction. The earliest u-filter data point in Fig. 3, obtained in this way, is in excellent agreement with the model prediction and it shows that the optical afterglow flux density was most likely rising at times $t \lesssim 5,000$ s.

XMM-Newton

We obtained two epochs of observations of the field of GRB 211211A with XMM-Newton at mid-times of about 9.6 d and about 50.9 d after the burst, lasting 40 ks and 67 ks in the pn CCD of the European Photon Imaging Camera (EPIC/pn), respectively. We relied on data products released through the Processing Pipeline Subsystem, with standard filtering for the background flares, resulting in 12.7-ks and 38.3-ks effective exposure time, respectively. Fully consistent results were obtained from an independent custom reduction carried out with the XMM-Newton Science Analysis Software. No clear X-ray source is detected at the afterglow position. From the resulting EPIC/pn images, we derive 3σ upper limits of about 3.6×10^{-3} counts per second and about 1.5×10^{-3} counts per second for the first and second epochs, respectively. Assuming the spectral parameters derived by Swift/XRT

(https://www.swift.ac.uk/xrt_spectra/01088940/), that is, Galactic absorption $N_{\text{H}} = 1.76 \times 10^{20} \text{ cm}^{-2}$ and photon index $\Gamma = 1.5$, these values translate into unabsorbed flux limits of about $1.1 \times 10^{-14} \text{ erg s}^{-1} \text{ cm}^{-2}$ and about $4.8 \times 10^{-15} \text{ erg s}^{-1} \text{ cm}^{-2}$ in the 0.3–10-keV energy range.

However, we report that running a targeted search at the GRB afterglow position on the first epoch of EPIC/pn data through the SOSTA (SOURCE STATISTICS) tool (part of the HEASOFT/XIMAGE software), a possible excess is detected with a count rate of $(3.2 \pm 1.0) \times 10^{-3}$ counts per second. Assuming the above spectral parameters, this translates into an unabsorbed 0.3–10-keV flux of $(1.02 \pm 0.32) \times 10^{-14} \text{ erg s}^{-1} \text{ cm}^{-2}$. However, given the low significance, it is not possible to assess whether this excess is owing to a real source or just to a spurious fluctuation. Considering this data point as an upper limit or a detection has no consequences for the conclusions of this paper.

Telescopio Nazionale Galileo

NIR observations of GRB 211211A were carried out with the Italian 3.6-m Telescopio Nazionale Galileo (TNG) telescope, sited in the Canary Islands, using the Near Infrared Camera Spectrometer (NICS) instrument in imaging mode. A series of images were obtained with the H filter on 16 December 2021 from 05:51:36 UT to 07:00:51 UT (that is, at a mid time of about 4.7 d after the burst). The image reduction was carried out using the jitter task of the European Southern Observatory (ESO) eclipse package (<https://www.eso.org/sci/software/eclipse/>). Astrometry was performed using the Two Micron All Sky Survey (2MASS, <https://irsa.ipac.caltech.edu/Missions/2mass.html>) catalogue. No source is detected at the optical and NIR counterpart position down to a 3σ upper limit of $H > 20.5$ mag (Vega) or $H > 21.9$ mag (AB).

Optical/NIR data

GRB 211211A has been followed up by numerous optical telescopes. We have selected observations in several bands (AB system) from the Gamma-Ray Coordinates Network (GCN) Circulars Archive for the afterglow modelling. We include in our analysis r-band data from the NEXT 0.6-m optical telescope³⁵, the Nordic Optical Telescope (NOT)³⁶, Multi-color Imaging Telescopes for Survey and Monstrous Explosions (MIT-SuME)³⁷, the Himalayan Chandra Telescope (HCT)³⁸, the Las Cumbres Observatory (LCO) 1-m Sinistro instrument³⁹, the Devasthal Optical Telescope⁴⁰ and the Zeiss-1000 telescope of Special Astrophysical Observatory of the Russian Academy of Sciences (SAO RAS)⁴¹; i-band data from the Calar Alto Faint Object Spectrograph (CAFOS/2.2-m) in Calar Alto Observatory (CAHA)^{42,43} and MITSuME³⁷; and k-band data from the Gemini-North Telescope⁴⁴. We show in Fig. 3 (green star at about 4,000 s) also the r-band flux density derived by converting a Katzman Automatic Imaging Telescope (KAIT) white filter observation⁴⁵ following ref.⁴⁶, but we conservatively do not include it in the modelling.

Very Large Array

Observations with the Karl G. Jansky VLA were performed 35 d (15 January 2022), 39 d (19 January 2022) and 77 d (26 February 2022) post-burst (principal investigator S.G.; project code 21B-370) at the central frequencies of 3 GHz (S band), 6 GHz (C band) and 10 GHz (X band), with a bandwidth of 2 GHz, 4 GHz and 4 GHz, respectively. The distance between the target and the phase calibrator (J1407+2827) is about 0.7°. Each observation started with scans of the flux and bandpass calibrator (J1331+3030). The data were calibrated using the custom Common Astronomy Software Applications (CASA) pipeline (version 6.2.1)⁴⁷ and visually inspected for possible radio-frequency interference. The final images were produced with the tclean task in CASA (version 5.1.0). We did not detect any point-like transient consistent with the Swift/XRT position of the burst.

Fermi/LAT

The LAT onboard Fermi is sensitive to the γ-ray photons in the energy band 0.1–300 GeV (ref.⁴⁸). We use the GTBURST tool to extract and

analyse the data. We define a region of interest (ROI) of 10° centred at the burst position (right ascension (RA) = 212.272° , declination (Dec.) = 27.884°) provided by Swift/BAT. We initially perform a standard LAT unbinned likelihood analysis. The null hypothesis is given by the baseline likelihood model, which includes the isotropic particle background ('isotr. template' in GTBURST), Galactic and extragalactic high-energy components from the Fermi Fourth Catalog (4FGL)⁴⁹, with fixed normalization ('template (fixed norm.)'). If a new source is present in the field of view (FOV), its addition to the model should describe the observed data better, given a certain position and spectral model. To assess whether the improvement is significant, we use the likelihood ratio test (LRT), as described in ref.⁵⁰. For each time bin, the LRT returns best-fit spectral values, as well as the relative test statistic $TS = -2 \times \ln(L_{\max,0}/L_{\max,i})$, where $L_{\max,0}$ is the maximum likelihood for the null hypothesis (background only), and $L_{\max,i}$ is the maximum likelihood for a model with the additional source at a given location and with a given spectral shape. In this analysis, we use the GRB position estimated by Swift/BAT and a power-law spectral model ('powerlaw2' using GTBURST).

The spectral parameters are only reported when the TS is larger than nine in a given time bin. The choice of the time bins is driven by the visibility of the source in the FOV of the telescope satisfying the condition of zenith angle below 100° and angular distance (source off-axis angle, θ) from the centre of the LAT FOV less than 60° . The values of zenith angle of 100° are chosen to minimize the effect of the Earth occultation.

We find only two time bins, 4–7 ks and 12–20 s after the trigger time ($t_0 = 660,921,004$ s Mission Elapsed Time (MET)) with $TS \geq 9$, whereas in the other time bins we obtain $TS < 9$, resulting in flux upper limits.

We choose the LAT data, to match the temporal bins covered by Swift/XRT. We select five epochs: 0.90–1.34 ks, 4–7 ks, 12–20 ks, 20–110 ks and 110–610 ks. We find that $TS \geq 9$ only between 4–7 ks and 12–20 ks, with a TS of 9 and 31 corresponding to about 3σ and about 5σ detections, respectively. For the first epoch, we estimate a flux $F_{LAT,1} = (5.8 \pm 4.0) \times 10^{-10}$ erg s $^{-1}$ cm $^{-2}$ (0.1–1 GeV) and a photon index $\Gamma_{LAT,1} = -2.8 \pm 0.7$, whereas for the second epoch $F_{LAT,2} = (5.1 \pm 2.0) \times 10^{-10}$ erg s $^{-1}$ cm $^{-2}$ and the photon index $\Gamma_{LAT,2} = -3.1 \pm 0.6$ (Fig. 1). We detected 9 photons from the GRB during the first 20 ks of observation with the probability of association with the GRB (p ; estimated with GTSRCPROB and P8R3_TRANSIENT010E_V2 as instrument response function) larger than 0.9. The standard criteria for detecting a GRB according to ref.⁵⁰ is to have more than 3 photons with $p > 0.9$. The highest-energy photon has been detected at 13 ks (at a position 0.32° away from the GRB location and with an associated probability of $p = 0.97$). This photon has an energy of 1.74 GeV. The properties of the photons, such as energy, GRB association probability, distance from the source and the arrival time from the trigger time are reported in Extended Data Table 1.

Finding the location of the gigaelectronvolt excess

We test the presence of a gigaelectronvolt source with the help of a TS map. In the TS map, we divide the ROI (12° around the GRB position) into several pixels with a side of 0.8° . We perform the same LAT likelihood analysis described in the previous section. We fix all spectral parameters, including the Galactic and isotropic diffuse emission templates⁵¹, except for the normalization factor of the spectra, which are left free to vary. The analysis returns a TS value for each pixel, assessing which are the positions in the ROI where the detected emission is coming from.

We applied this strategy to three time bins: one day before, one day after and the day of the GRB 211211A trigger. As this analysis explores a longer time duration than 200 s, the event class P8R3_TRANSIENT010E_V2 is used as mentioned in ref.⁵⁰. We performed an LRT by considering the time intervals only when the border of the ROI is at a zenith angle less than 100° , which reduces the contamination from the Earth limb.

We show the results in Fig. 1. We obtain a maximum $TS \approx 43$ in the TS map made during the first 20 ks after the burst, resulting in a $>5\sigma$ detection, in spatial coincidence with the GRB, hence confirming the

existence of the gigaelectronvolt source. Conversely, in the day before and after the burst, the maximum TS does not reach 9 in coincidence with the burst position.

Ruling out external high-energy contamination

The ROI of GRB 211211A includes 5 sources within 5° from the burst location: 4FGL J1410.4+2820, 4FGL J1417.9+2543, 4FGL J1424.1+2917, 4FGL J1351.9+2847 and 4FGL J1350.8+3033, with distances of 0.55° , 2.93° , 3.59° , 3.87° and 4.79° , respectively. Among these sources, 4FGL J1410.4+2820 is located at a distance of 0.5° , which is smaller than the LAT point spread function 68% containment angle (about 1° at 1 GeV; ref.⁵²). This source is associated with RX J1410.4+2821 (RA = 212.623° , Dec. = 28.342°), a BL Lacertae object (BL Lac)⁵³. To rule out the possibility that the gigaelectronvolt photons detected at the location of the GRB are associated with a flaring state of the BL Lac object and estimate the possible contamination in our detection by the BL Lac flux, we analysed the data of the BL Lac object 4FGL J1410.4+2820 using the ENRICO TOOLS⁵⁴. We selected P8R3_SOURCE_V2 as the response function. We used events from 0.1 GeV to 300 GeV selected within a 10° ROI centred at 4FGL J1410.4+2820 and having a zenith distance below 100° to avoid contamination from the Earth's limb. The diffuse Galactic and isotropic components were modelled with the files 'gll_iem_v07.fits' and 'iso_P8R3_SOURCE_V2.txt', respectively. We included the point sources in the 4FGL located in the 10° ROI and an additional surrounding 5° -wide annulus. The spectral slopes were fixed to their 4FGL values, whereas the normalization of the sources within the ROI as well as the diffuse components are kept free to vary. We analysed monthly binned data of the BL Lac object before the trigger time of the GRB (658,293,004–660,921,004 s MET) and after (661,007,404–663,635,404 s MET) excluding one day around the GRB burst (660,921,004–661,007,404 s MET). The spectral analysis of the BL Lac for one month before and after the trigger returns upper limits of values 7×10^{-13} erg s $^{-1}$ cm $^{-2}$ and 2×10^{-12} erg s $^{-1}$ cm $^{-2}$, respectively. These upper limits are about two orders of magnitude smaller than the flux obtained from the LAT excess in temporal coincidence with the GRB. We also included the time-averaged broadband spectrum of the BL Lac in 12 years of observation (https://fermi.gsfc.nasa.gov/ssc/data/access/lat/12yr_catalog; Extended Data Fig. 1)⁵⁵, which is consistent with the flux upper limits derived from the monthly binned data from the BL Lac object.

Comparisons with other LAT emissions from GRBs

The first sGRB detected by Fermi/LAT, GRB 090510 ($z = 0.9$; ref.⁵⁶), was observed in the gigaelectronvolt band during the first 1,000 s of observation and then the emission fades away with no detectable emission at later time (after 1 ks). GRBs emitting high-energy radiation detected by Fermi/LAT are collected in the second Fermi/LAT GRB Catalog (2FLGC,²⁷). The catalogue contains about 200 sources starting from Fermi launch up to the end of 2018, for a total of 10 years. We compare the GRB 211211A with the populations of IGRBs and sGRBs in the catalogue. Our classification of long or short bursts is based on the duration T_{90} estimate provided by Fermi/GBM. We consider only emissions that reach $TS \geq 9$ in the time-resolved analysis performed in ref.²⁷.

By comparing the fluxes in the 0.1–10 GeV energy band (Fig. 2a), we note that GRB 211211A observations lie in the tail of light curves of the IGRB population. If we consider the isotropic-equivalent LAT luminosity L_{iso} (Fig. 2b) for a sub-sample of GRBs with redshift measurements, we observe that this emission is significantly fainter with respect to both short and long populations. This suggests that the LAT emission of GRB 211211A is intrinsically fainter, and it would be hardly detectable for sources placed at larger distances (that is, >350 Mpc).

In Extended Data Fig. 2a, we compare the prompt duration of the burst T_{90} with the time at which LAT started to detect high-energy (HE) emission from the GRB. GRB 211211A occupies the top-right corner of

Article

the plot, together with other IGRBs showing LAT late-time emission. In Extended Data Fig. 2b, we compare flux in the energy range 0.1–10 GeV and spectral index obtained through a time-integrated analysis along all the LAT duration. We observe that GRB 211211A occupies a region of the plot relatively far from the clustered region occupied by IGRBs and the sparse distribution of sGRBs.

Search for similar gigaelectronvolt component in nearby GRBs

Four GRBs closer than 350 Mpc have been detected by Swift/BAT and Fermi/GBM so far: GRB 111005A, GRB 100316D, GRB 171205A and GRB 190829A with redshifts of 0.013, 0.059, 0.037 and 0.078, respectively. GRB 100316D, GRB 171205A and GRB 190829A are typical IGRBs with associated supernovae observed. The LAT data analysis for these three GRBs shows no detection from the source within one day from the trigger time. The corresponding upper limits are the following: 1.15×10^{-10} erg s $^{-1}$ cm $^{-2}$, 1.35×10^{-10} erg s $^{-1}$ cm $^{-2}$ and 1.38×10^{-10} erg s $^{-1}$ cm $^{-2}$, respectively. GRB 111005A is an IGRB⁵⁷ without an associated supernova. The Fermi/LAT observations for this GRB also result in flux upper limits of 7.9×10^{-10} erg s $^{-1}$ cm $^{-2}$, 9×10^{-10} erg s $^{-1}$ cm $^{-2}$, 1.8×10^{-10} erg s $^{-1}$ cm $^{-2}$, 1.78×10^{-10} erg s $^{-1}$ cm $^{-2}$ and 1.74×10^{-10} erg s $^{-1}$ cm $^{-2}$ for the five consecutive days after the trigger ($t_0 = 339,494,716.22$ MET). The sGRB GRB 170817A, associated with the BNS merger event GW170817, was not detected by LAT during the gravitational-wave trigger as the telescope was transiting through the South Atlantic Anomaly, preventing to put constraints on the high-energy component at the time of the merger. At later times (from minutes to days after the BNS merger), the LAT observations do not show any detection but enable to place flux upper bounds²⁸. In the time bin between 1,153 s and 2,027 s after the gravitational-wave trigger, an upper limit of 4.5×10^{-10} erg s $^{-1}$ cm $^{-2}$ was estimated in the 0.1–1-GeV energy range corresponding to an equivalent isotropic luminosity upper limit of 9.7×10^{43} erg s $^{-1}$. In the same time interval, we have a flux upper limit whose corresponding luminosity upper limit is two orders of magnitude brighter than the one measured for GW170817. Instead, in the time interval of our gigaelectronvolt detection, Fig. 3 in ref.²⁸ shows a flux upper limit which is on the order of 10^{-9} erg s $^{-1}$ cm $^{-2}$. By correcting for the distances, the flux of GRB 211211A for a source at the same distance as GW170817 would have been brighter than this upper limit. The gigaelectronvolt emission discovered for GRB 211211A was not present in GW170817. This can be explained within our scenario interpreting the gigaelectronvolt emission; GW170817 was observed off-axis (a viewing angle of about 15° from the jet) where the EIC emission is expected to be severely suppressed owing to relativistic beaming. In addition, the very dense kilonova ejecta could absorb most of the off-axis gigaelectronvolt emission via the Bethe–Heitler process, further preventing its detection for off-axis observers.

Forward-shock model

The GRB emission is thought to be produced within a collimated, relativistic outflow (that is, a jet) that moves in a direction close to the line of sight (for example, ref.⁵⁸). As the jet expands into the interstellar medium (ISM) at above the local sound speed, a forward shock forms and propagates in the ISM (for example, refs.^{59,60}). We model the dynamics and emission of the forward shock, assuming the line of sight to be on the jet axis and the ISM to be homogeneous with number density n , following ref.⁶¹, with the only minor difference that we model the lateral expansion of the shocked region following the recipe from ref.⁶² instead of assuming sound-speed expansion as in ref.⁶¹. Although the difference in the light curves obtained with the two methods is very small, we found the sound-speed model to produce slight discontinuities in the derivative of some light curves, which we believe is an artefact. The emission model includes both synchrotron and SSC from electrons accelerated at the forward shock, but we find that, for our best-fit parameters, the SSC contribution is negligible in the relevant bands. In the model, a fraction χ_e of the ISM electrons that cross the shock is assumed to be accelerated to relativistic speeds. Accelerated electrons

are assumed to be injected into the shocked fluid with a Lorentz factor γ distribution $d\eta/dy \propto \gamma^{-p}$ for $\gamma \geq \gamma_m$, with γ_m being the minimum Lorentz factor, to hold a fraction ϵ_e of the shocked fluid energy density and to be subject to cooling owing to synchrotron and SSC emission (the cooling due to the latter is computed including Klein–Nishina effects). Small-scale turbulence is assumed to produce an effectively isotropic magnetic field that holds a constant fraction ϵ_B of the shocked fluid energy density. The model is entirely determined by eight parameters, namely the jet isotropic-equivalent kinetic energy E , its bulk Lorentz factor Γ and half-opening angle θ_j , the ISM number density n , and the ‘microphysical’ parameters ϵ_e , ϵ_B , χ_e and p .

Kilonova model

During and after the merger of a binary of two compact objects including at least one neutron star (NS), outflows of neutron-rich material can be produced by a variety of mechanisms. Ejecta that remain cold (that is, are not heated by shocks) and do not receive intense neutrino irradiation retain an extremely low proton fraction $Y_e = n_p/(n_n + n_p) \lesssim 0.05$ (for example, ref.⁶³, where n_p and n_n are the number densities of protons and neutrons, respectively). Tidal forces (especially acting on the least-massive component of the binary) can unbind cold material, mainly along the orbital plane and over millisecond timescales, with high speeds (0.1–0.3 c), potentially large masses (up to $0.1 M_\odot$) and low Y_e (refs.^{63,64}); in the case of a BNS merger, shocks at the colliding surfaces of the two NS can eject low amounts ($\lesssim 10^{-3} M_\odot$) of comparably high-speed material, with high Y_e , preferentially along the polar direction; again in the BNS case, if the merger does not lead to a prompt collapse to a black hole, violent oscillations and/or bar modes in the immediate post-merger remnant can produce copious mass ejection (a few $\times 10^{-2} M_\odot$) of neutrino-irradiated material with relatively high Y_e (ref.⁶⁵); last, but not least, winds driven by neutrino energy deposition (leading to high Y_e) and more prominently by viscous angular momentum transport (leading to a broad range of Y_e values) in the accretion disk around the merger remnant can unbind a large fraction (about 10–30%) of the disk mass, with relatively low speeds $\lesssim 0.1$ (for example, refs.^{66,67}).

During the first stages of expansion, nucleosynthesis by rapid neutron capture (r-process) takes place within these outflows. If Y_e is sufficiently low (about $Y_e \lesssim 0.2$; for example, ref.⁶⁸) heavy r-process elements (lanthanides and actinides) can be produced. Their complex valence electron structure results in an extremely high opacity to photons in the infrared-to-ultraviolet wavelength range⁶⁹. As a result, outflows that start off with $Y_e \lesssim 0.2$ are expected to have extremely high opacities $\kappa \gtrsim 10 \text{ cm}^2 \text{ g}^{-1}$ and thus long diffusion times. Lanthanide-free outflows (those initially with $Y_e \gtrsim 0.2$) are instead expected to have lower opacities $0.5 \lesssim \kappa (\text{cm}^2 \text{ g}^{-1}) \lesssim 3$. Regardless of the presence of lanthanides, the radioactive decay (mainly beta) of unstable isotopes in these outflows is thought to constitute a heating source for the ejecta with a robust heating rate that depends very weakly on the exact composition⁷⁰. Such heating is the power source of the so-called kilonova emission that is produced as these outflows expand^{15,71}.

In the modelling behind this work, we did not attempt at capturing the complexity of the kilonova emission in the presence of several outflows with different masses, speeds, opacities and geometries, given the insufficient detail in the available data. We instead opted for adopting the simple, semi-analytical, one-component, isotropic model from ref.⁷². This model is entirely specified by three parameters, namely the ejecta mass m_{ej} , maximum speed $v_{max,ej}$ and constant grey opacity κ .

The inferred kilonova ejecta mass is $m_{ej} = 2.0^{+0.9}_{-0.6} \times 10^{-2} M_\odot$, expanding with an average velocity of $v_{ej} \approx 0.5 v_{max,ej} = 0.10^{+0.07}_{-0.04} c$ (refs.^{72,73}) and with a relatively low opacity $\kappa = 0.6^{+0.8}_{-0.3} \text{ cm}^2 \text{ g}^{-1}$. These properties are compatible with winds from a hyper-massive proto-neutron star remnant (HMNS)⁷⁴. Alternatively, such ejecta properties are in general agreement with those expected from material ejected due to enhanced angular momentum transport in the highly rotating, oblate remnant owing to the formation of spiral arms (the ‘spiral wave wind’ described

in ref.⁶⁵). Both interpretations favour the hypothesis that the merger remnant passed through a HMNS phase before collapsing. A black-hole–neutron-star scenario seems less favoured with respect to a BNS merger, especially owing to the velocity of the low-opacity component which, in a black-hole neutron-star merger, would have to be produced in the form of winds from the accretion disk around the merger remnant, but with a substantially lower expected velocity $v_{\text{ej}} \approx 0.03 - 0.06 c$ (ref.⁷⁵).

Model fitting

We fit our 11-parameter model (8 parameters for the forward shock and 3 for the kilonova) to the available light-curve data as follows. Let us define our observations as a set of N_{ν} flux densities $\{F_{\nu,i}\}_{i=1}^{N_{\nu}}$ measured at radio, NIR, optical and ultraviolet frequencies at the i -th time t_i , and a set of fluxes F and photon indices α $\{F_i, \alpha_i\}_{i=1}^{N_F}$ measured in X-rays and γ-rays. Each flux density measurement contributes an additive term to our log-likelihood, which reads, in the case of detections

$$\log \mathcal{L}_{F_{\nu},i} = -\frac{1}{2} \frac{(F_{\nu,\text{m},i}(t_i) - F_{\nu,i})^2}{\sigma_i^2} - \frac{1}{2} \ln(2\pi\sigma_i^2), \quad (1)$$

where $F_{\nu,\text{m},i}(t_i)$ is the flux density predicted by the model at the corresponding time and frequency, and $\sigma_i = \sqrt{\sigma_{\text{obs},i}^2 + f_{\text{sys}}^2 F_{\nu,\text{m},i}^2}$ is the assumed uncertainty, which is the sum square of the formal uncertainty $\sigma_{\text{obs},i}$ associated with the observation and an unknown systematic contribution to the error, parameterized by the dimensionless constant f_{sys} (which therefore constitutes an additional model parameter). The normalization term (the second term on the right-hand side of equation (1)) is included as it effectively represents a penalty for higher values of f_{sys} . In the case of upper limits, our log-likelihood term becomes a simple one-sided Gaussian penalty, namely

$$\log \mathcal{L}_{\text{UL},i} = -\frac{1}{2} \frac{\{\max[(F_{\nu,\text{m},i}(t_i) - F_{\nu,i}), 0]\}^2}{(0.01F_{\nu,i})^2}. \quad (2)$$

For X-ray and γ-ray fluxes, the additive term is

$$\log \mathcal{L}_{F,i} = -\frac{1}{2} \frac{(F_{\text{m},i}(t_i) - F_i)^2}{\sigma_i^2} - \frac{1}{2} \ln(2\pi\sigma_i^2) - \frac{1}{2} \frac{(\alpha_{\text{m},i}(t_i) - \alpha_i)^2}{\sigma_{\alpha,i}^2}, \quad (3)$$

where again $\sigma_i = \sqrt{\sigma_{\text{obs},i}^2 + f_{\text{sys}}^2 F_{\text{m},i}^2}$ as for the flux densities, $\sigma_{\alpha,i}$ is the uncertainty on the observed photon index (we assume no systematic uncertainty on the photon index) and the model photon index $\alpha_{\text{m},i}$ is simply defined as the average of the slope of the model photon spectrum over the instrument band. Adopting log-uniform priors on all parameters except p (for which we use a uniform prior), within the bounds given in Extended Data Table 2, we sampled the posterior probability density with a Markov chain Monte Carlo approach using the emcee Python package⁷⁶, employing $N_{\text{walk}} = 4 \times N_{\text{dim}} = 48$ walkers (where $N_{\text{dim}} = 12$ is the dimension of the parameter space). We initialized the walkers in a small N_{dim} -dimensional ball around a point in our parameter space representing ‘standard’ GRB afterglow parameters, $x = (52.5, 0, 2, -1, -1, -3, 0, 2.1, -2, 0, -1, -1)$ where x represents the parameters as listed in Extended Data Table 2, and we performed $N_{\text{iter}} = 10,000$ iterations, for a total of $N_{\text{iter}} \times N_{\text{walk}} = 480,000$ samples. The final mean autocorrelation time is about 600, and the posterior looks reasonably smooth and single-peaked. As a cross-check, we also run several shorter ($N_{\text{iter}} \approx 2,000$) chains with different starting parameters, and these all converged to the same parameter space region after a burn in. A corner plot demonstrating the features of our posterior is shown in Extended Data Fig. 3, and summary information on the parameter credible ranges from the marginalized posteriors is reported in Extended Data Table 2. Most parameters are relatively well constrained, except for the ISM density, whose posterior rails against the prior bound and it can therefore be only constrained to be $n (\text{cm}^{-3}) < 10^{-4.2}$ (95% credible level, consistent with the large offset from the host galaxy and the absence of

local absorption), and the fraction of accelerated electrons, that can only be constrained to be $\chi_e < 0.3$ (95% credible level, in agreement with expectations from particle-in-cell simulations, for example, ref.⁷⁷).

External inverse Compton

To explain the high-energy (100 MeV–1 GeV) excess at 10^4 s found for GRB 211211A with respect to the standard synchrotron and SSC model of the afterglow, we invoke emission by EIC. EIC scattering of soft seed photons by hot electrons in relativistic jets has been considered for a long time to explain the high-energy emission in blazars⁷⁸. Signatures of the EIC cooling of electrons in the GRB afterglow phase have been proposed by different authors. Prompt emission photons can be Comptonized in the reverse⁷⁹ and forward shock⁸⁰ of the blast wave. The EIC radiation from upscattered prompt emission^{81,82}, X-ray^{83–86} or ultraviolet flares⁸⁷, a dense ambient infrared photon field⁸⁸, by the forward-shock-accelerated electrons can give a rise of the gigaelectronvolt radiation. The photons from the supernova shock break out⁸³ or cocoon^{85,89–92} are also considered as seed photons for the EIC in the forward shock site or in the internal dissipation site, including also late-time dissipation related to the X-ray plateau emission (see ref.⁹³ for a general overview).

Given that the Fermi/LAT spectrum is soft and the afterglow spectrum at lower energies (X-ray) is rising in νF_{ν} (Fig. 3b), the EIC spectral component should be preferably narrow, favouring thermal seed photons. As late as 10^4 s after the GRB, the rise of the kilonova makes its photons the natural and viable candidate seed photon source.

We first consider EIC scattering of the kilonova photons by hot electrons produced in the forward shock. To do so, we estimate the size R_{FS} , bulk Lorentz factor Γ_{FS} and the typical electron Lorentz factor $\gamma_{\text{m,FS}}$ at the forward shock, at time T after the GRB, using the parameters close to the best-fit parameters of the afterglow model:

$$\Gamma_{\text{FS}} = 58 E_{53}^{1/8} n_{-4}^{-1/8} T_4^{-3/8}, \quad (4)$$

$$R_{\text{FS}} = 4 \times 10^{18} E_{53}^{1/4} n_{-4}^{-1/4} T_4^{1/4} \text{ cm}, \quad (5)$$

$$\gamma_{\text{m,FS}} = 8 \times 10^3 \epsilon_{e,-1.5} \chi_{e,-1}^{-1} E_{53}^{1/8} n_{-4}^{-1/8} T_4^{-3/8}, \quad (6)$$

where Q_x stands for $Q/10^x$ in cgs units, Q being any of the model parameters.

Given the large radius of the forward shock, most of the seed photons are received from behind; therefore, the energy density of the seed photons in the comoving frame of the forward-shock region can be approximated as

$$U'_{\text{seed}} = \frac{L_{\text{seed}}}{4\pi R_{\text{FS}}^2 \Gamma_{\text{FS}}^2 c}. \quad (7)$$

The Lorentz factor of electrons cooling via the EIC on a dynamical timescale of $R_{\text{FS}}/(\Gamma_{\text{FS}}c)$ (where c is the speed of light) is

$$\gamma_{\text{c,EIC}} = \frac{3\pi m_e c^3 R_{\text{FS}} \Gamma_{\text{FS}}^3}{\sigma_T L_{\text{seed}}} \approx 10^{13} E_{53}^{5/8} n_{-4}^{-5/8} T_4^{-7/8} \quad (8)$$

clearly indicating that efficient extraction of energy from forward-shock-accelerated electrons through the EIC process is impossible: the kilonova luminosity of $L_{\text{seed}} \approx 10^{40} \text{ erg s}^{-1}$ is too low to account for the observed approximately 100-MeV component with $L_{\text{excess}} \approx 5 \times 10^{45} \text{ erg s}^{-1}$. If there were any other source of NIR/optical seed photons with the required luminosity, at 10^4 s, it would overshine the observed optical afterglow emission.

Therefore, to account for the high-energy emission by the EIC, we need to invoke a source of hot electrons at much smaller radii.

Article

As a heuristic explanation, we assume a low-power jet to be present at the relevant late times (Fig. 5). This is not novel in GRBs: many IGRBs and sGRBs are followed by late-time X-ray flares^{94–96} and plateau emission^{97,98}. These emission components are widely thought^{99,100} to be linked to late-time internal dissipation in a long-lived jet, which in compact binary mergers can be produced either by a highly magnetized and fast-spinning proto-magnetar remnant^{101,102} or by fallback accretion¹⁰³.

Therefore, we assume the presence of a source of hot electrons in the jet, which we call the ‘dissipation site’, in the vicinity of the kilonova ejecta. In this scenario, we can constrain the parameters of the dissipation site by the following requirements: (1) the seed photons for the EIC scattering are the kilonova photons, and (2) the dissipation in the low-power jet should not overshine the observed optical and the X-ray afterglow emission by its synchrotron and SSC radiation.

We define L_j , Γ_j and R_j as the luminosity, bulk Lorentz factor and dissipation radius of the low-power jet, respectively. $\chi_e = 0.1\chi_{e,-1}$ is the fraction of the N_e jet electrons accelerated at the jet dissipation site, with an energy distribution of $dN_e/dy \propto y^p$ and a minimum Lorentz factor, assuming $p = 2.5$, of

$$\gamma_m \approx 610 \frac{\epsilon_{e,-1}}{\chi_{e,-1}} (\Gamma' - 1), \quad (9)$$

where Γ' is the relative bulk Lorentz factor of one shell relative to another (assuming internal-shock-driven dissipation of jet kinetic energy).

Relativistic electrons in the jet lose their energy through synchrotron radiation, SSC and EIC on a timescale (in the jet comoving frame)

$$t'_c = \frac{\gamma m_e c^2}{P'_{\text{syn}} + P'_{\text{SSC}} + P'_{\text{EIC}}} = \frac{3m_e c}{4\sigma_T \gamma [U'_B + U'_{\text{syn}} + U'_{\text{ext}}]}, \quad (10)$$

where U'_B , U'_{syn} and U'_{ext} are the magnetic, synchrotron photon and external photon energy densities in the comoving reference frame, respectively; P'_{syn} , P'_{SSC} and P'_{EIC} are the synchrotron, SSC and EIC emitted powers, respectively; m_e is the electron mass; σ_T is the Thomson cross section; and we are assuming that both SSC and EIC happen in the Thomson regime. The Lorentz factor of electrons that cool efficiently on a dynamical timescale $t'_{\text{dyn}} = R_j/(c\Gamma_j)$ is given by

$$\gamma_c = \frac{3m_e c^2 \Gamma_j}{4\sigma_T R_j} [U'_B + U'_{\text{syn}} + U'_{\text{ext}}] = \frac{\gamma_c^{\text{syn}}}{1 + \frac{U'_{\text{syn}}}{U'_B} + \frac{U'_{\text{ext}}}{U'_B}}, \quad (11)$$

where $\gamma_c^{\text{syn}} = (3m_e c^2 \Gamma_j)/(4\sigma_T R_j U'_B)$ is the Lorentz factor of hypothetical electrons cooling via synchrotron radiation only.

We introduce two microphysical parameters: the fraction of shock downstream energy density carried by the magnetic field B' , $\epsilon_B = B'^2 R_j^2 c / (2L_j)$, and the fraction carried by relativistic electrons, $\epsilon_e \approx 0.1$, with a total power in non-thermal electrons given by $L_e = \epsilon_e L_j$.

As a first attempt, we assume the dissipation site to be above the kilonova photosphere, whose radius is $R_{\text{KN}} \approx 6 \times 10^{13} \nu_{\text{max,ej},-0.7} T_4$ cm, with T being the temporal parameter. In this configuration, where $R_j > R_{\text{KN}}$ (scenario A), most of the seed photons from the kilonova are de-beamed as seen in the jet comoving frame.

In that frame, the external photon energy density from the kilonova is given by

$$U'_{\text{ext}} = \frac{L_{\text{seed}}}{4\pi R_j^2 c \Gamma_j^2}, \quad (12)$$

where the kilonova luminosity is $L_{\text{seed}} \approx 3 \times 10^{40} \text{ erg s}^{-1}$ at $t = 10^4$ s.

Assuming EIC to be the dominant cooling process, the Lorentz factor of electrons that cool via the EIC on a dynamical timescale of $R_j/(c\Gamma_j)$ is

$$\gamma_{\text{c,EIC}} = \frac{3\pi m_e c^3 R_j \Gamma_j^3}{\sigma_T L_{\text{seed}}} \approx 3 \times 10^4 R_{j,14} \Gamma_{j,0.7}^3. \quad (13)$$

In this scenario, it is reasonable to assume a slow-cooling regime for the injected electrons, that is, $\gamma_m < \gamma_{\text{c,EIC}}$. By requiring the peak of the EIC to be at about 100 MeV, we get an estimate for the jet bulk Lorentz factor, namely

$$\Gamma_j \approx 3 L_{\text{seed},40.5}^{1/3} R_{j,13.8}^{-1/3} \left(\frac{\nu_{\text{EIC}}/\nu_{\text{seed}}}{10^8} \right)^{1/6}. \quad (14)$$

The observed luminosity is dominated by the electrons that cool at $R_j/(c\Gamma_j)$, that is

$$L_{\text{EIC}} \approx \tau_T \left(\frac{\gamma_c}{\gamma_m} \right)^{3-p} \gamma_m^2 L_{\text{seed}}, \quad (15)$$

where τ_T is the Thomson optical depth at the dissipation site, which can be estimated as

$$\tau_T \approx \frac{\sigma_T L_j \chi_e}{4\pi R_m c^3 \Gamma_j^3}. \quad (16)$$

Here m_p is the proton mass. This returns $L_{\text{EIC}} \approx 10^{45} L_{\text{seed},40.5}^{p-2} R_{j,47} \chi_{e,-1}^{p-1} R_{j,13.8}^{2-p} \Gamma_{j,0.5}^{6-3p} \text{ ergs}^{-1}$, where the numerical values hereon are given for $p = 2.5$.

If we assume the electrons at the dissipation site to be accelerated by internal shocks with a Lorentz factor contrast of about Γ , then the fraction of internal energy carried by the accelerated electrons in the shock downstream is $\epsilon_e \approx 0.08 \gamma_{m,3} \chi_{e,-1} / (\Gamma_{j,0.5} - 1)$.

This configuration is able to match the excess observed in the high-energy band of this source, but it requires unrealistic microphysical conditions: the requirement that the EIC dominates over synchrotron, that is, $U'_{\text{ext}} > U'_B$, implies

$$\epsilon_B < \frac{L_{\text{seed}}}{L_j} < \frac{L_{\text{seed}} \eta_{\text{rad}}}{L_{\text{LAT}}} \approx 3 \times 10^{-6}, \quad (17)$$

where $\eta_{\text{rad}} = \frac{L_{\text{LAT}}}{L_{\text{EIC}} + L_j} \approx \frac{L_{\text{LAT}}}{L_j} \approx 0.1$ and $U'_B = \epsilon_B L_j / (4\pi R_j^2 c \Gamma_j^2)$. So, given the very low luminosity of the kilonova seed photons and the observed LAT luminosity of this gigaelectronvolt source, the required magnetization of the low-power jet is very low.

By requiring that EIC is also dominant with respect to SSC, that is, $U'_{\text{ext}} > U'_{\text{syn}}$, we find an even stronger constraint: the energy density in the photons produced by the synchrotron radiation is

$$U'_{\text{syn}} = \frac{L'_{\text{syn}}}{4\pi R_j^2 c}. \quad (18)$$

By considering the cooling of electrons at γ_c and taking into account the shape of the electron distribution, we obtain

$$\epsilon_B \lesssim \frac{12\pi m_p c^3 R_j \Gamma_j}{L_j^2 \chi_e \sigma_T \left(\frac{\gamma_c}{\gamma_m} \right)^{3-p} \gamma_m^2} L_{\text{seed}} \approx 3 \times 10^{-10} R_{14} \Gamma_{j,0.7}^{-2} L_{j,47}^{-2} \chi_{e,-1}^{-1} \gamma_{c,m,1}^{-0.5} \gamma_{m,1}^{-2} \quad (19)$$

where $\gamma_{c/m} = \gamma_c/\gamma_m$ and $L'_{\text{syn}} \approx \tau_T \left(\frac{\gamma_c}{\gamma_m} \right)^{3-p} \gamma_m^2 \epsilon_B L_j$.

One can not increase ϵ_B by increasing $R_{14} \Gamma_{j,0.7}^3$ because it would shift the observed peak of the EIC to higher energies (equation (13)). We notice that in this scenario, one cannot invoke EIC fast cooling (to increase ϵ_B by two orders of magnitude by extracting all the energy in electrons), as it would require that $\Gamma' > \Gamma_j$.

We consider a second scenario where the dissipation site is below the kilonova photosphere, that is, $R_j < R_{KN}$, allowing the photons to be beamed in the jet comoving frame. In this case (scenario B), the external photon energy density is given by

$$U'_{\text{ext}} = \frac{L_{\text{seed}} \Gamma_j^2}{4\pi R_j^2 c}. \quad (20)$$

We note that in this scenario, the electrons must be in the fast cooling regime, as $\gamma_{c,\text{EIC}} \approx 10R_{j,13} \Gamma_{j,1}^{-1} \ll \gamma_m$, so that the peak of the EIC spectral energy will be provided by electrons at γ_m , that is

$$\frac{\nu_{\text{EIC}}}{\nu_{\text{seed}}} \approx 2\gamma_m^2 \Gamma_j^2. \quad (21)$$

By requiring that EIC dominates over synchrotron emission ($U'_{\text{ext}} > U'_B$), we obtain

$$\epsilon_B < \frac{L_{\text{seed}} \Gamma_j^4}{L_j} \approx 3 \times 10^{-2} \Gamma_{j,1}^4 L_{j,46}^{-1}, \quad (22)$$

where we used a lower reference jet power, because we have an energy budget of $\epsilon_B L_j$ in the fast cooling regime. We adopt $\Gamma_j \approx 10$ to provide a 100-MeV peak of EIC, as $\gamma_m \approx 1,000$ for approximately a few Γ' .

By requiring that EIC dominates over SSC ($U'_{\text{ext}} > U'_{\text{syn}}$), we obtain

$$\epsilon_B < 8 \times 10^{-6} R_{j,13} \Gamma_{j,1}^5 L_{j,46}^{-2} \chi_{e,-1}^{-1} \gamma_m^{-2}. \quad (23)$$

Therefore, also in this scenario the magnetic field in the shock downstream must be low, with $\epsilon_B \lesssim 10^{-6}$.

Inwards diffusion of kilonova photons towards the low-power jet

For kilonova photons to be available for up-scattering within the low-power jet, and for them to be seen as beamed in the dissipation site comoving frame, the transverse photon diffusion time must be smaller than the dynamical time in a sizable fraction of the kilonova ejecta with mass density ρ above R_j . To show that this is the case, let $\tau_\perp \approx \kappa \rho(v, t) v t \theta$ be the transverse optical depth in a portion of angular size θ of the kilonova ejecta Lagrangian shell with velocity v . The corresponding diffusion time is $t_{\text{diff},\perp} = v t \theta \tau_\perp / c$. Setting this equal to the dynamical time t , we then obtain the angular distance $\theta_{\text{diff}}(v, t) = \sqrt{c / (\kappa \rho(v, t) v^2 t)}$ over which transverse diffusion is effective at a time t or, as a more informative product, the fraction $f_{\text{diff}}(v, t) \approx 1 - \cos(\theta_{\text{diff}}(v, t))$ of the kilonova ejecta solid angle (assumed isotropic for simplicity) over which the transverse diffusion is effective. In our kilonova ejecta model, which follows ref.⁷², the density profile is given by $\rho(v, t) = \rho_0 (t/t_0)^3 (1 - (v/v_{\max,\text{ej}})^2)^3$, where t_0 is a reference time and $\rho_0 \approx (315/16) m_{\text{ej}} / (4\pi v_{\max,\text{ej}}^3 t_0^3)$ is the density normalization. Taking the ejecta heating rate due to the decay of unstable heavy isotopes produced by r-process nucleosynthesis to be $70 \dot{e}(t) \approx \dot{e}_0 (t/10^4 \text{ s})^{-1.3}$ with $\dot{e}_0 = 1.8 \times 10^{11} \text{ erg s}^{-1} \text{ g}^{-1}$, the luminosity that can diffuse inwards above a radius R_j is then obtained approximately from

$$L_{\text{KN,in}}(>R_j, t) \approx \dot{e}(t) \int_{R_j/t}^{v_{\text{ph}}(t)} 4\pi t^3 v^2 \rho(v, t) f_{\text{diff}}(v, t) dv, \quad (24)$$

where $v_{\text{ph}}(t)$ is the Lagrangian position of the radial photosphere, and we are following ref.⁷² in removing the emission from above the photosphere, as the thermalization efficiency of nuclear decay products there is expected to be very low. The value of the above integral at $t = 10^4 \text{ s}$, as a function of R_j and assuming our best-fit parameters $m_{\text{ej}} = 0.02 M_\odot$ and $\kappa = 0.6 \text{ cm}^2 \text{ g}^{-1}$, is shown in Extended Data Fig. 4a.

The evolution of $L_{\text{KN,in}}$ as a function of time, assuming $R_j = 10^{13} \text{ cm}$, is shown in Extended Data Fig. 4b. For comparison, we also show the total kilonova luminosity from the model. This demonstrates that

most of the kilonova luminosity is available for up-scattering close to the peak, and also explains the expected time evolution of the EIC component.

As a final note, we neglected the presence of an expanding cocoon in between the jet and the kilonova ejecta. We note here that (1) the cocoon is composed of kilonova material, and hence will undergo the same heating due to r-process product decay as the kilonova ejecta, and (2) the cocoon is expected to be less massive and faster than the kilonova ejecta themselves, and therefore its contribution to the transverse optical depth is unimportant. Inwards diffusion of its cooling emission could contribute to the photon field available for up-scattering, but given the absence of an observed cooling emission at these times, this component is probably subdominant anyway. We therefore conservatively keep only the kilonova ejecta as our source of seed photons.

Time-dependent semi-analytical model for the EIC component

The analytical investigations in the previous sections indicate that the EIC scattering of kilonova photons in a low-power jet could be a viable scenario to explain the observed excess on top of the forward-shock synchrotron emission at 0.1–1 GeV at around 10^4 s . Therefore, we set out to explore such a scenario more in detail by setting up a simple semi-analytical model that enables us to predict the light curves and spectra of such a component. We assumed the jet to remain active after the end of the prompt emission, with a decaying isotropic-equivalent kinetic luminosity $L_j = L_{j,0} (t/T)^{-a}$ and bulk Lorentz factor $\Gamma_j = \Gamma_{j,0} (t/T)^{-b}$, with $L_{j,0} \approx 6 \times 10^{51} \text{ erg s}^{-1}$ (where $T \approx 34 \text{ s}$ is the prompt emission duration as measured by Fermi/GBM and $L_{j,0} \approx E/T$) and $\Gamma_{j,0} \approx 1,200$ (from our afterglow modelling). On the basis of the expectation that marginally bound material from the tidally disrupted least-massive NS in the progenitor binary will keep falling back¹⁰³ and feed an accretion disk with an accretion rate $\dot{M} \propto t^{-5/3}$ (ref.¹⁰⁴), we set $a = 5/3$, whereas $b > 0$ remains as a free parameter. Under these assumptions, we can compute at any time the radius of the jet photosphere from¹⁰⁵ $R_{\text{ph}} \approx \kappa_{\text{es}} L_j / (8\pi \Gamma_j^3 c^3) \approx 10^9 (t/T)^{3b-5/3} \text{ cm}$ where we took the electron scattering opacity $\kappa_{\text{es}} = 0.2 \text{ cm}^2 \text{ g}^{-1}$, appropriate for a $Y_e = 1/2$ electron fraction. Given the very large Lorentz factor and relatively small luminosity, the photosphere therefore starts off very deep in the jet. We assume dissipation events (specifically, internal shocks) to happen randomly throughout the jet from the photosphere up, with an optimistic Lorentz factor contrast $\Gamma' \approx \Gamma_j$, so that electrons are accelerated with a power-law energy distribution $dn_e/dy \propto y^{-p}$ at the dissipation site above an injection Lorentz factor $\gamma_m = 1 + (p-2)/[(p-1)(\epsilon_e/\chi_e)(m_p/m_e)(\Gamma_j - 1)]$, within an isotropic-equivalent comoving volume $V' \approx 4\pi R_j^3 / \Gamma_j$. We assume the dominant EIC emission to come from kilonova photons upscattered at a radius $R_j \approx \max(R_{\text{ph}}, R_{KN})$, where the latter quantity indicates the kilonova photosphere. Whenever $R_{\text{ph}} < R_{KN}$, we assume the kilonova photons to have energies Doppler-boosted by a factor Γ_j in the comoving frame of the jet, so that their energy density in that frame, at the dissipation site, is $U'_{\text{ext}} = \Gamma_j^2 L_{KN} / (4\pi R_j^2 c)$. Conversely, if $R_{\text{ph}} > R_{KN}$, then we assume the photons to be de-beamed, so that $U'_{\text{ext}} = \Gamma_j^2 L_{KN} / (4\pi R_j^2 c)$. Accordingly, the kilonova temperature, as seen in the jet comoving frame is $T'_{\text{ext}} = \Gamma_j^s T_{KN}$ with $s = 1$ if $R_{\text{ph}} < R_{KN}$ and $s = -1$ otherwise. The relativistic electrons in the jet dissipation site emit (and cool) by synchrotron, SSC and EIC: the cooling Lorentz factor γ_c , at which the cooling time equals the dynamical time, is obtained by solving numerically the implicit equation

$$\gamma_c (1 + Y_{\text{EIC}} + Y_{\text{SSC}}(\gamma_c)) = \frac{6\pi m_e c^2 \Gamma_j}{\sigma_T B'^2 R_j}, \quad (25)$$

where $Y_{\text{EIC}} = U'_{\text{ext}} / U'_B$ and $Y_{\text{SSC}}(\gamma_c) \approx n_e' P_{v,\text{syn,max}} v'_0 / U'_B$, with $P_{v,\text{syn,max}} = \sigma_T m_e c^2 B' / (3e)$, $n_e' \approx \chi_e L_{j,\text{iso}} / (4\pi R_j^2 \Gamma_j^2 m_p c^3)$ and $v'_0 = \max(\gamma_m^2, \gamma_c^2) e B' / (2\pi m_e c)$, and assuming the usual parameterization $U'_B = \epsilon_B L_{j,\text{iso}} / (4\pi R_j^2 \Gamma_j^2 c)$. All these assumptions completely specify the electron and photon energy distributions in the comoving frame. Given these, we compute the

Article

EIC emissivity in the low-power jet as $j'_{v,EIC} = [hv/(4\pi)][d^2n'_v/(dv dt)]$, where h is the Planck constant and the comoving density of photons emitted per unit time is

$$\frac{d^2n'_v}{dv dt} = \int_{\min(\gamma_m, \gamma_c)}^{\infty} \frac{d^2N_{v,EIC}}{dv dt}(v', T'_{ext}, \kappa_d) \frac{dn'_e}{dy} dy. \quad (26)$$

We compute the EIC specific photon scattering rate per electron $d^2N_{v,EIC}/(dv dt)$ adopting the simple analytical approximation from ref.¹⁰⁶ (their equation (14)), using a dilution factor $\kappa_d = \Delta\Omega/(4\pi) \approx [R_j/(2R_{KN})]^2 = 1/4$ (this is a conservative choice, as the actual kilonova solid angle $\Delta\Omega$, as seen in the jet comoving frame, is possibly larger than π) and a temperature $T'_{ext} = \Gamma_j^{ST} T_{KN}$. The electron Lorentz factor distribution is assumed to have the usual form⁶⁰

$$\frac{dn'_e}{dy} \propto \begin{cases} (\gamma/\gamma_0)^{-q} & \gamma_p \leq \gamma \leq \gamma_0 \\ (\gamma/\gamma_0)^{-p-1} & \gamma > \gamma_0 \end{cases}, \quad (27)$$

where $\gamma_p = \min(\gamma_m, \gamma_c)$, $\gamma_0 = \max(\gamma_m, \gamma_c)$, $q = p$ if $\gamma_m \leq \gamma_c$ and $q = 2$ otherwise. The normalization is such that $\int (dn'_e/dy) dy = N_e/V' = \chi_e L_j / (4\pi R_j^2 \Gamma_j^2 m_p c^3)$. We then compute the final EIC specific luminosity as

$$\frac{dL_{EIC}}{dv} = \Gamma_j^2 V' j'_{v,EIC} f_{jet} \quad (28)$$

where $f_{jet} = \min(1, \Gamma_j^2 \theta_j^2)$ accounts for the reduction in the observed luminosity when $\Gamma_j < \theta_j^{-1}$, and we use $\theta_j = 1^\circ$ as found from the afterglow modelling.

The resulting model has five free parameters, namely $b, \epsilon_e, \epsilon_b, p$ and χ_e . We found that $b = 0.6, \epsilon_e = \chi_e = 0.1, \epsilon_b = 10^{-8}$ and $p = 2.2$ provides a viable solution, that reproduces both the LAT light curve and the spectral energy density distributions (SEDs; Fig. 5), with the jet synchrotron emission remaining below the forward-shock one, as shown in Extended Data Fig. 5.

The evolution of the EIC component shown in Fig. 5 is the combined result of the evolution of the jet power and Lorentz factor, the kilonova luminosity and temperature, and the energy density of the kilonova photons as seen in the jet comoving frame at the dissipation radius. The latter determines the contribution of EIC to the cooling of electrons accelerated at the dissipation region, which affects the shape of the effective electron energy distribution that produces the EIC emission upon scattering of the kilonova photons.

Comparison with afterglow models from other studies

GRB 211211A has been analysed by several other groups^{3,26,107}. The preferred afterglow model parameters reported in these studies are different from ours. To address this discrepancy, we produced the same diagnostic plots as in Fig. 3, but using their best-fit parameters, and adopting the afterglowpy¹⁰⁸ software (which allows for off-axis viewing angles and structured jets, as opposed to our modelling, which assumes the line of sight to be on the jet axis, and the jet properties to be uniform within the jet opening angle). As shown in Extended Data Figs. 6–8, the parameters reported in the previous studies typically lead to predictions that match the multi-wavelength light curves at $t \gtrsim 10^4$ s, but fail to reproduce the early optical data and the XRT photon index (except for ref.²⁶, whose model has the correct photon index in the XRT band). Similarly to our model, the model from ref.²⁶ produces a similar flux to the observed one in the LAT band in correspondence of the first detection, but with an inconsistent photon index. All models (including ours; Fig. 3) instead are well below the second LAT detection, further supporting its interpretation as an excess over the synchrotron afterglow.

Recently, ref.¹⁰⁹ independently analysed the Fermi/LAT data and confirmed the gigaelectronvolt detection of GRB 211211A. Their flux

values are similar to the ones estimated in the present work. However, there are significant differences in data and modelling as detailed in the following. Their Fig. 3 shows the first upper limit starting at 400 s and covering about 1.5 ks. However, up to 1 ks, the source was off-axis ($\theta > 65^\circ$) with respect to the LAT FOV and no upper limit can be reliably estimated in this interval. In addition to that, their interpretation, which attributes the late high-energy emission to synchrotron radiation from the forward shock, uses only an arbitrary subset of the available data, especially in the infrared-to-ultraviolet (UVOIR) bands. This, together with the fact that their numerical afterglow model is not publicly available (and we are not able to reproduce their result using our own model, which could be attributed to differences in the details of the implementation) makes it difficult to assess independently whether their interpretation is really viable (we note, however, that their initial Lorentz factor is in a region with very little posterior support according to our results; Extended Data Fig. 3). In that case, the early optical observation by UVOT would then have to be explained separately.

Data availability

Swift/XRT raw data are public and available from the UK Swift Science Data Centre at the University of Leicester. The light-curve data were taken from https://www.swift.ac.uk/xrt_curves/GRB_ID/flux.qdp, where GRB_ID is the GRB observation ID. The spectra were obtained from https://www.swift.ac.uk/xrt_spectra/addspec.php?targ=GRB_ID where GRB_ID is the GRB observation ID. The details of the automatic spectral analysis can be found at https://www.swift.ac.uk/xrt_spectra/docs.php. Swift/UVOT raw data are available at <https://heasarc.gsfc.nasa.gov/cgi-bin/W3Browse/swift.pl>. Fermi/LAT raw data are public and can be downloaded using the software GTBURST available at <https://fermi.gsfc.nasa.gov/ssc/data/analysis/scitoools/gtburst.html>. The Fermi/LAT second GRB catalogue data are available at https://www-glast.stanford.edu/pub_data/953/. The VLA data are available at the public repository <https://data.nrao.edu/portal/#/>. The observation code is 21B-370. XMM-Newton raw data are available at <https://www.cosmos.esa.int/web/xmm-newton/xsa>. The TNG data are available from the corresponding author upon reasonable request.

Code availability

HEASOFT, XSPEC and PYXSPEC are freely available online at <https://heasarc.gsfc.nasa.gov/docs/software/heasoft/>, <https://heasarc.gsfc.nasa.gov/xanadu/xspec/> and <https://heasarc.gsfc.nasa.gov/docs/xanadu/xspec/python/html/index.html>. GTBURST is part of the Fermi Science Tools package, freely available at <https://fermi.gsfc.nasa.gov/ssc/data/analysis/software/>. The details of the GTBURST analysis can be found at <https://fermi.gsfc.nasa.gov/ssc/data/analysis/scitoools/gtburst.html>. The XMM-Newton Science Analysis Software is freely available at <https://www.cosmos.esa.int/web/xmm-newton/sas-download>. SOSTA is part of the XIMAGE software package, freely available at <https://heasarc.gsfc.nasa.gov/xanadu/ximage/ximage.html>. The ESO eclipse package is available at <https://www.eso.org/sci/software/eclipse/>. The CASA software is available at https://casa.nrao.edu/casa_obtaining.shtml. A tutorial on how to use CASA can be found at https://casaguides.nrao.edu/index.php?title=VLA_Continuum_Tutorial_3C391-CASA6.2.0. emcee is a Python package, available at <https://emcee.readthedocs.io/en/stable/user/install/>. AFTERGLOWPY is a Python package, available at <https://github.com/geoffryan/afterglowpy>. All reduced data and computer code are available from the corresponding author upon reasonable request.

31. Evans, P. A. et al. Methods and results of an automatic analysis of a complete sample of Swift-XRT observations of GRBs. *Mon. Not. R. Astron. Soc.* **397**, 1177–1201 (2009).

32. Kalberla, P. M. W. et al. The Leiden/Argentine/Bonn (LAB) Survey of Galactic HI. Final data release of the combined LDS and IAR surveys with improved stray-radiation corrections. *Astron. Astrophys.* **440**, 775–782 (2005).
33. Belles, A. & D'Ai, A. GRB 211211A: Swift/UVOT detection. *GRB Coord. Netw. Circ.* No. 31222 (2021).
34. Schlafly, E. F. & Finkbeiner, D. P. Measuring reddening with Sloan Digital Sky Survey stellar spectra and recalibrating SFD. *Astrophys. J.* **737**, 103 (2011).
35. Jiang, S. Q. et al. GRB 211211A: Nanshan/NEXT optical observations. *GRB Coord. Netw. Circ.* No. 31213 (2021).
36. Malesani, D. B. et al. GRB 211211A: NOT optical spectroscopy. *GRB Coord. Netw. Circ.* No. 31221 (2021).
37. Ito, N. et al. GRB 211211A: MITSUME Akeno optical observation. *GRB Coord. Netw. Circ.* No. 31217 (2021).
38. Kumar, H. et al. GRB 211211A: HCT and GIT optical follow up observations. *GRB Coord. Netw. Circ.* No. (2021).
39. Strausbaugh, R. & Cucchiara, A. GRB 211211A: LCO optical observations. *GRB Coord. Netw. Circ.* No. 31214 (2021).
40. Gupta, R. et al. GRB 211211A: observations with the 3.6m Devasthal Optical Telescope. *GGRB Coord. Netw. Circ.* No. 31299 (2021).
41. Moskvitin, A. et al. GRB 211211A: SAO RAS optical observations. *GRB Coord. Netw. Circ.* No. 31234 (2021).
42. de Ugarte Postigo, A. et al. GRB 211211A: afterglow detection from CAFOS/2.2m CAHA. *GRB Coord. Netw. Circ.* No. 31218 (2021).
43. de Ugarte Postigo, A. et al. GRB 211211A: further observations from CAFOS/2.2m CAHA. *GRB Coord. Netw. Circ.* No. 31228 (2021).
44. Levan, A. J. et al. GRB 211211A—Gemini K-band detection. *GRB Coord. Netw. Circ.* No. 31235 (2021).
45. Zheng, W. & Filippenko, A. V. GRB 211211A: KAIT optical afterglow candidate. *GRB Coord. Netw. Circ.* No. 31203 (2021).
46. Li, W., Filippone, A. V., Chornock, R. & Jha, S. The Katzman Automatic Imaging Telescope gamma-ray burst alert system, and observations of GRB 020813. *Publ. Astron. Soc. Pac.* **115**, 844–853 (2003).
47. McMullin, J. P., Waters, B., Schiebel, D., Young, W. & Golap, K. CASA architecture and applications. In *Astronomical Data Analysis Software and Systems XVI: Astronomical Society of the Pacific Conference Series* Vol. 376 (eds Shaw, R. A. et al.) 127 (2007).
48. Ackermann, M. et al. The first Fermi-LAT catalog of sources above 10 GeV. *Astrophys. J. Suppl. Ser.* **209**, 34 (2013).
49. Abdollahi, S. et al. Fermi Large Area Telescope fourth source catalog. *Astrophys. J. Suppl. Ser.* **247**, 33 (2020).
50. Ajello, M. et al. A decade of gamma-ray bursts observed by Fermi-LAT: the second GRB catalog. *Astrophys. J.* **878**, 52 (2019).
51. Abdalla, H. et al. A very-high-energy component deep in the γ-ray burst afterglow. *Nature* **575**, 464–467 (2019).
52. Ajello, M. et al. Fermi Large Area Telescope performance after 10 years of operation. *Astrophys. J. Suppl. Ser.* **256**, 12 (2021).
53. Massaro, F. et al. The gamma-ray blazar quest: new optical spectra, state of art and future perspectives. *Astrophys. Space Sci.* **361**, 337 (2016).
54. Sanchez, D. A. & Deli, C. Enrico: a Python package to simplify Fermi-LAT analysis. In *International Cosmic Ray Conference: International Cosmic Ray Conference* Vol. 33, 2784 (2013).
55. Fermi-LAT collaboration Incremental Fermi Large Area Telescope fourth source catalog. *Astrophys. J. Suppl. Ser.* **260**, 53 (2022).
56. Ackermann, M. et al. Fermi observations of GRB 090510: a short-hard gamma-ray burst with an additional, hard power-law component from 10 keV to GeV energies. *Astrophys. J.* **716**, 1178–1190 (2010).
57. Michałowski, M. J. et al. The second-closest gamma-ray burst: sub-luminous GRB 111005A with no supernova in a super-solar metallicity environment. *Astron. Astrophys.* **616**, A169 (2018).
58. Kumar, P. & Zhang, B. The physics of gamma-ray bursts & relativistic jets. *Phys. Rep.* **561**, 1–109 (2015).
59. Sari, R., Piran, T. & Narayan, R. Spectra and light curves of gamma-ray burst afterglows. *Astrophys. J.* **497**, L17–L20 (1998).
60. Panaitescu, A. & Kumar, P. Analytic light curves of gamma-ray burst afterglows: homogeneous versus wind external media. *Astrophys. J.* **543**, 66–76 (2000).
61. Salafia, O. S. et al. Multi-wavelength view of the close-by GRB 190829A sheds light on gamma-ray burst physics. *Astrophys. J.* **931**, L19 (2022).
62. Granot, J. & Piran, T. On the lateral expansion of gamma-ray burst jets. *Mon. Not. R. Astron. Soc.* **421**, 570–587 (2012).
63. Hotokezaka, K. et al. Mass ejection from the merger of binary neutron stars. *Phys. Rev. D* **87**, 024001 (2013).
64. Radice, D. et al. Binary neutron star mergers: mass ejection, electromagnetic counterparts, and nucleosynthesis. *Astrophys. J.* **869**, 130 (2018).
65. Nedora, V. et al. Spiral-wave wind for the blue kilonova. *Astrophys. J.* **886**, L30 (2019).
66. Just, O., Bauswein, A., Ardevol Pulpillo, R., Goriely, S. & Janka, H. T. Comprehensive nucleosynthesis analysis for ejecta of compact binary mergers. *Mon. Not. R. Astron. Soc.* **448**, 541–567 (2015).
67. Siegel, D. M. & Metzger, B. D. Three-dimensional GRMHD simulations of neutrino-cooled accretion disks from neutron star mergers. *Astrophys. J.* **858**, 52 (2018).
68. Lippuner, J. & Roberts, L. F. r-process lanthanide production and heating rates in kilonovae. *Astrophys. J.* **815**, 82 (2015).
69. Kasen, D., Badnell, N. R. & Barnes, J. Opacities and spectra of the r-process ejecta from neutron star mergers. *Astrophys. J.* **774**, 25 (2013).
70. Korobkin, O., Rosswog, S., Arcones, A. & Winteler, C. On the astrophysical robustness of the neutron star merger r-process. *Mon. Not. R. Astron. Soc.* **426**, 1940–1949 (2012).
71. Metzger, B. D. Kilonovae. *Living Rev. Relativ.* **23**, 1 (2019).
72. Grossman, D., Korobkin, O., Rosswog, S. & Piran, T. The long-term evolution of neutron star merger remnants—II. Radioactively powered transients. *Mon. Not. R. Astron. Soc.* **439**, 757–770 (2014).
73. Wollaeger, R. T. et al. Impact of ejecta morphology and composition on the electromagnetic signatures of neutron star mergers. *Mon. Not. R. Astron. Soc.* **478**, 3298–3334 (2018).
74. Ciolfi, R. & Kalinani, J. V. Magnetically driven baryon winds from binary neutron star merger remnants and the blue kilonova of 2017 August. *Astrophys. J.* **900**, L35 (2020).
75. Fernández, R., Foucart, F. & Lippuner, J. The landscape of disc outflows from black hole-neutron star mergers. *Mon. Not. R. Astron. Soc.* **497**, 3221–3233 (2020).
76. Foreman-Mackey, D., Hogg, D. W., Lang, D. & Goodman, J. emcee: the MCMC hammer. *Publ. Astron. Soc. Pac.* **125**, 306 (2013).
77. Spitkovsky, A. Particle acceleration in relativistic collisionless shocks: Fermi process at last? *Astrophys. J.* **682**, L5 (2008).
78. Dermer, C. D. & Schlickeiser, R. Model for the high-energy emission from blazars. *Astrophys. J.* **416**, 458 (1993).
79. Beloborodov, A. M. Optical and GeV-TeV flashes from gamma-ray bursts. *Astrophys. J.* **618**, L13–L16 (2005).
80. Fan, Y. Z., Zhang, B. & Wei, D. M. Early photon-shock interaction in a stellar wind: a sub-GeV photon flash and high-energy neutrino emission from long gamma-ray bursts. *Astrophys. J.* **629**, 334–340 (2005).
81. Murase, K., Toma, K., Yamazaki, R., Nagataki, S. & Ioka, K. High-energy emission as a test of the prior emission model for gamma-ray burst afterglows. *Mon. Not. R. Astron. Soc.* **402**, L54–L58 (2010).
82. Murase, K., Toma, K., Yamazaki, R. & Mészáros, P. On the implications of late internal dissipation for shallow-decay afterglow emission and associated high-energy gamma-ray signals. *Astrophys. J.* **732**, 77 (2011).
83. Wang, X.-Y., Li, Z. & Mészáros, P. GeV-TeV and X-ray flares from gamma-ray bursts. *Astrophys. J.* **641**, L89–L92 (2006).
84. Fan, Y.-Z., Piran, T., Narayan, R. & Wei, D.-M. High-energy afterglow emission from gamma-ray bursts. *Mon. Not. R. Astron. Soc.* **384**, 1483–1501 (2008).
85. Zhang, B. T., Murase, K., Yuan, C., Kimura, S. S. & Mészáros, P. External inverse-Compton emission associated with extended and plateau emission of short gamma-ray bursts: application to GRB 160821B. *Astrophys. J.* **908**, L36 (2021).
86. Murase, K. et al. Double neutron star mergers and short gamma-ray bursts: long-lasting high-energy signatures and remnant dichotomy. *Astrophys. J.* **854**, 60 (2018).
87. Fan, Y. & Piran, T. Sub-GeV flashes in γ-ray burst afterglows as probes of underlying bright far-ultraviolet flares. *Mon. Not. R. Astron. Soc.* **370**, L24–L28 (2006).
88. Zhang, H., Christie, I. M., Petropoulou, M., Rueda-Becerril, J. M. & Giannios, D. Inverse Compton signatures of gamma-ray burst afterglows. *Mon. Not. R. Astron. Soc.* **496**, 974–986 (2020).
89. Toma, K., Wu, X.-F. & Mészáros, P. An up-scattered cocoon emission model of gamma-ray burst high-energy lags. *Astrophys. J.* **707**, 1404–1416 (2009).
90. Kumar, P. & Smoot, G. F. Some implications of inverse-Compton scattering of hot cocoon radiation by relativistic jets in gamma-ray bursts. *Mon. Not. R. Astron. Soc.* **445**, 528–543 (2014).
91. De Colle, F., Lu, W., Kumar, P., Ramirez-Ruiz, E. & Smoot, G. Thermal and non-thermal emission from the cocoon of a gamma-ray burst jet. *Mon. Not. R. Astron. Soc.* **478**, 4553–4564 (2018).
92. Kimura, S. S. et al. Upscattered cocoon emission in short gamma-ray bursts as high-energy gamma-ray counterparts to gravitational waves. *Astrophys. J.* **887**, L16 (2019).
93. Zhang, B. *The Physics of Gamma-Ray Bursts* (Cambridge Univ. Press, Cambridge, 2018).
94. Burrows, D. N. et al. Bright X-ray flares in gamma-ray burst afterglows. *Science* **309**, 1833–1835 (2005).
95. Falcone, A. D. et al. The giant X-ray flare of GRB 050502B: evidence for late-time internal engine activity. *Astrophys. J.* **641**, 1010–1017 (2006).
96. Chincarini, G. et al. The first survey of X-ray flares from gamma-ray bursts observed by Swift: temporal properties and morphology. *Astrophys. J.* **671**, 1903–1920 (2007).
97. Nousek, J. A. et al. Evidence for a canonical gamma-ray burst afterglow light curve in the Swift XRT data. *Astrophys. J.* **642**, 389–400 (2006).
98. Liang, E.-W., Zhang, B.-B. & Zhang, B. A comprehensive analysis of Swift XRT data. II. Diverse physical origins of the shallow decay segment. *Astrophys. J.* **670**, 565–583 (2007).
99. Zhang, B. et al. Physical processes shaping gamma-ray burst X-ray afterglow light curves: theoretical implications from the Swift X-ray telescope observations. *Astrophys. J.* **642**, 354–370 (2006).
100. Ghisellini, G., Ghirlanda, G., Nava, L. & Firmani, C. "Late prompt" emission in gamma-ray bursts? *Astrophys. J.* **658**, L75–L78 (2007).
101. Dai, Z. G. & Lu, T. Gamma-ray burst afterglows and evolution of postburst fireballs with energy injection from strongly magnetic millisecond pulsars. *Astron. Astrophys.* **333**, L87–L90 (1998).
102. Zhang, B. & Mészáros, P. Gamma-ray burst afterglow with continuous energy injection: signature of a highly magnetized millisecond pulsar. *Astrophys. J.* **552**, L35–L38 (2001).
103. Rosswog, S.Fallback accretion in the aftermath of a compact binary merger. *Mon. Not. R. Astron. Soc.* **376**, L48–L51 (2007).
104. Rees, M. J. Tidal disruption of stars by black holes of 10^6 – 10^8 solar masses in nearby galaxies. *Nature* **333**, 523–528 (1988).
105. Daigne, F. & Mochkovitch, R. The expected thermal precursors of gamma-ray bursts in the internal shock model. *Mon. Not. R. Astron. Soc.* **336**, 1271–1280 (2002).
106. Khangulyan, D., Aharonian, F. A. & Kelner, S. R. Simple analytical approximations for treatment of inverse Compton scattering of relativistic electrons in the blackbody radiation field. *Astrophys. J.* **783**, 100 (2014).
107. Yang, J. et al. A long-duration gamma-ray burst with a peculiar origin. *Nature* <https://doi.org/10.1038/s41586-022-05403-8> (2022).
108. Ryan, G., van Eerten, H., Piro, L. & Troja, E. Gamma-ray burst afterglows in the multimessenger era: numerical models and closure relations. *Astrophys. J.* **896**, 166 (2020).
109. Zhang, H.-M., Huang, Y.-Y., Zheng, J.-H., Liu, R.-Y. & Wang, X.-Y. Fermi-LAT detection of a GeV afterglow from a compact stellar merger. *Astrophys. J.* **933**, L22 (2022).

Article

Acknowledgements We thank A. Celotti, G. Ghisellini, A. Segreto, E. Ambrosi and M. Grazia Bernardini for discussions. The National Radio Astronomy Observatory is a facility of the National Science Foundation operated under cooperative agreement by Associated Universities, Inc. P.D. and S.C. thank N. ScharTEL for granting XMM-Newton DDT observations. M.B. acknowledges financial support from the Italian Ministry of University and Research (MUR, PRIN 2020 grant 2020KB33TP). M.B. and G.O. acknowledge financial support from the AHEAD2020 project (grant agreement number 871158). B.B., M.B. and P.D. acknowledge financial support from MUR (PRIN 2017 grant 20179Z5K5KS). O.S.S. thanks MUR grant 2017MB8AEZ for financial support. P.D. and S.C. acknowledge support from ASI grant I/004/11/5. This work made use of data supplied by the UK Swift Science Data Centre at the University of Leicester.

Author contributions A.M., B.B. and G.O. carried out LAT data reduction and analysis, and lead the GeV discovery. O.S.S. performed the multi-wavelength afterglow modelling. G.O. and O.S.S. developed the theoretical model used to interpret the high-energy excess. A.M., B.B., G.O. and O.S.S. lead the paper writing. G.G., M.B., S.G., P.D. and S.R. gave significant inputs on data interpretation. M.B. and G.G. gave major contributions to the paper writing. All authors

contributed to discussions and editing of the paper. P.D. is the principal investigator of the XMM-Newton observations, and collected and analysed the optical and UV data. P.D. and S.C. reduced and analysed the XMM data and edited the corresponding text in the paper. S.G. is the principal investigator of the VLA observations. He reduced and analysed the radio data, and edited the corresponding text in the paper. P.T. and A.S. contributed to the LAT analysis providing computational tools. B.B. produced Fig. 1 and Extended Data Fig. 1. A.M. produced Fig. 2 and Extended Data Fig. 2. O.S.S. produced Figs. 3 and 5 and Extended Data Figs. 3–8. S.R. produced Fig. 5.

Competing interests The authors declare no competing interests.

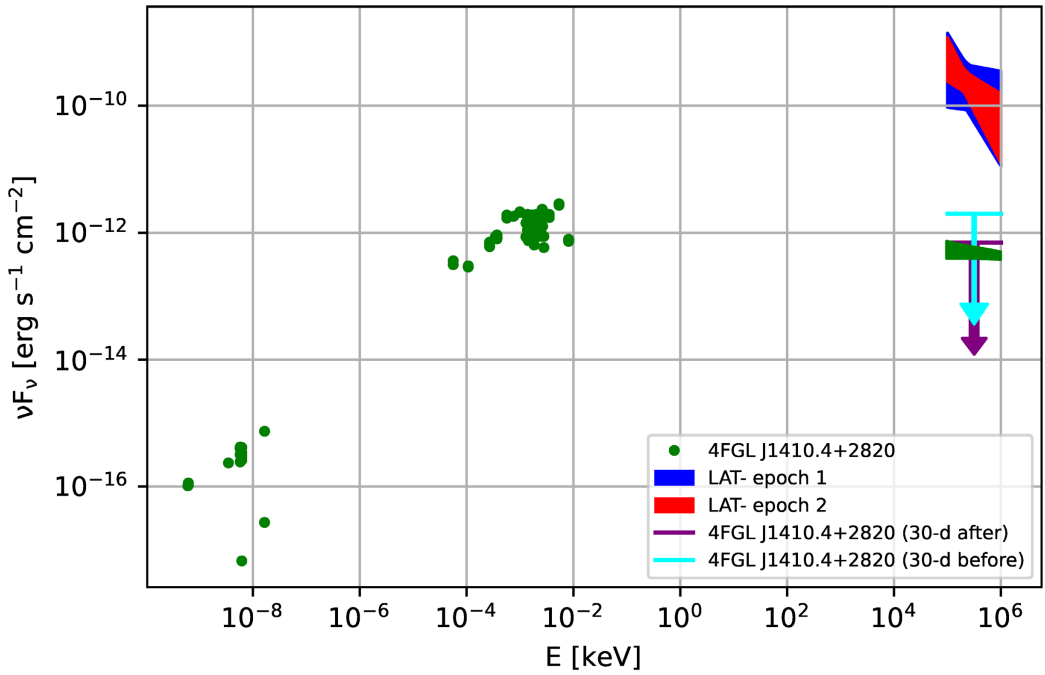
Additional information

Supplementary information The online version contains supplementary material available at <https://doi.org/10.1038/s41586-022-05404-7>.

Correspondence and requests for materials should be addressed to Alessio Mei.

Peer review information *Nature* thanks Gregoire Marcel and the other, anonymous, reviewer(s) for their contribution to the peer review of this work. Peer reviewer reports are available.

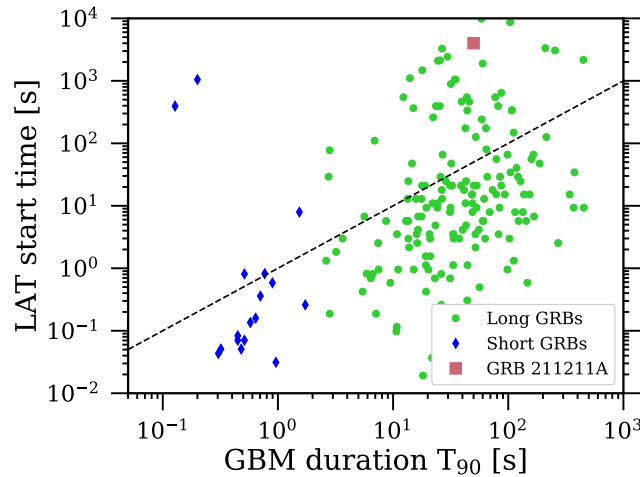
Reprints and permissions information is available at <http://www.nature.com/reprints>.



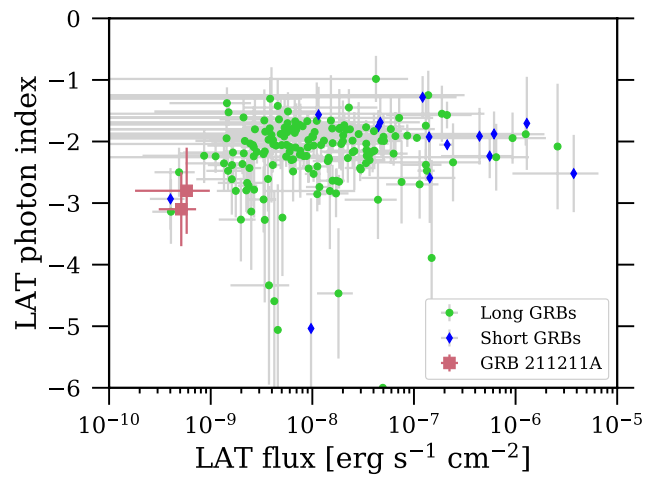
Extended Data Fig. 1 | Time-averaged broadband spectrum of 4FGL

J1410.4+2820. The two arrows represent the 3σ upper limits for the BL Lac flux obtained using one month of observation by Fermi/LAT before and after the GRB (in yellow and purple, respectively). The green band in the GeV energies

represents the time-averaged GeV emission from 12 years of observation⁵⁵. The emission from the blazar is at least two orders of magnitude weaker than the emission from the GRB.



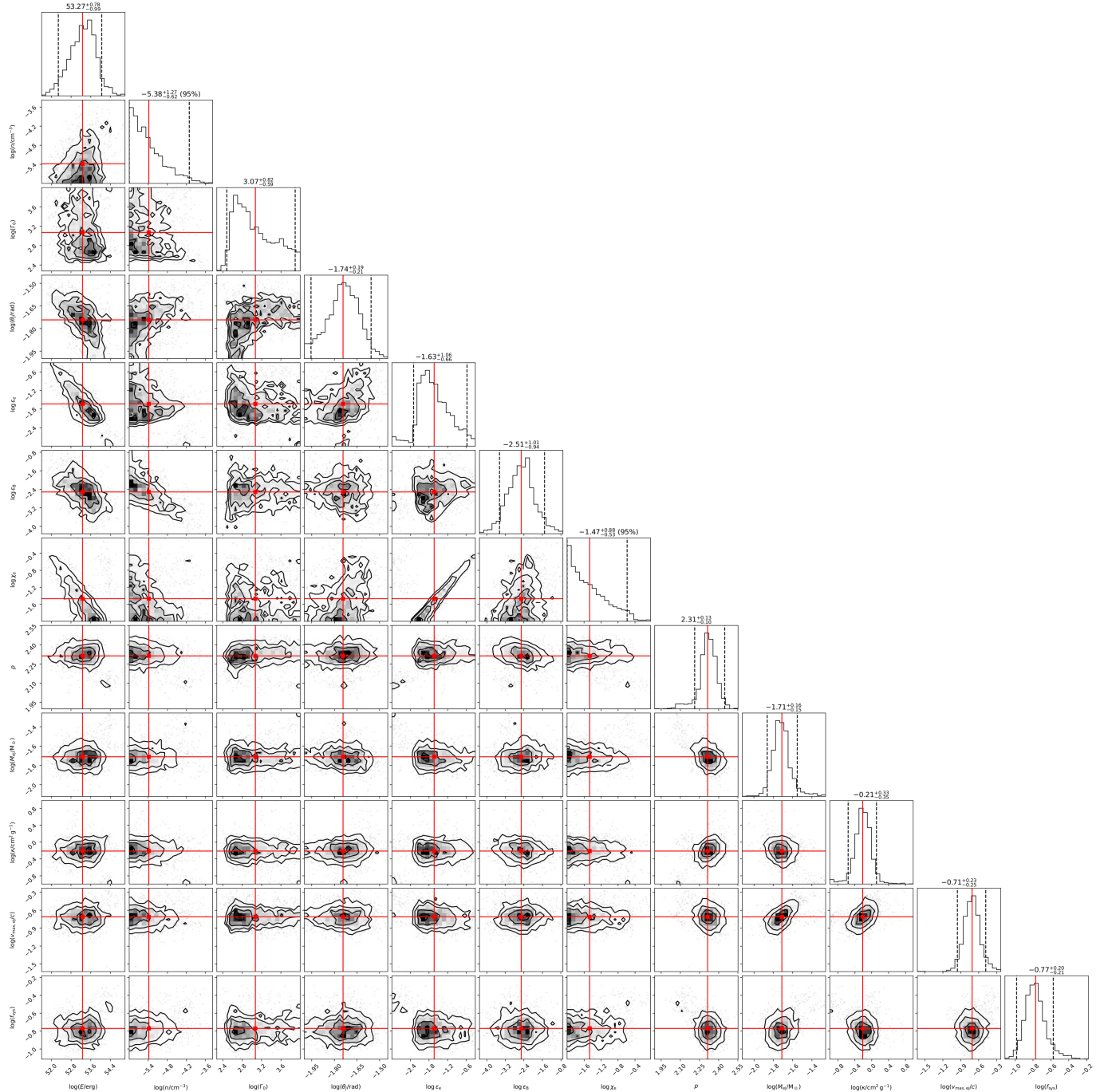
(a)



(b)

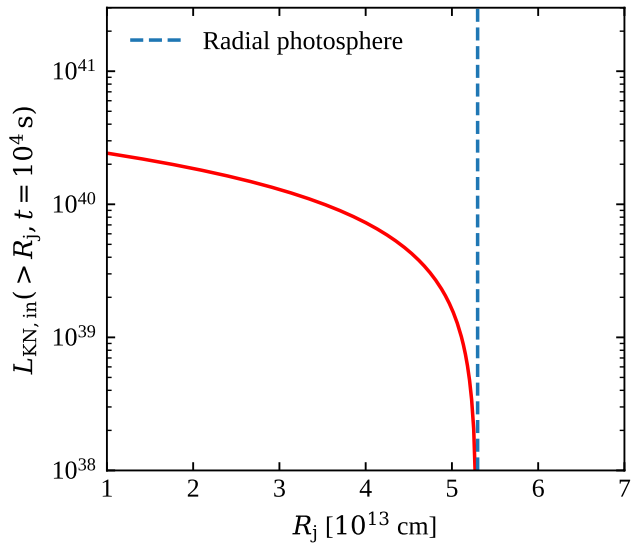
Extended Data Fig. 2 | Comparisons with other GRBs observed by Fermi/LAT. Long (in green) and short (in blue) bursts emissions from the second Fermi/LAT GRB catalogue²⁷ compared to GRB 211211A (in brown). **a**, LAT detection time from the burst versus the GRB duration T_{90} computed with Fermi/GBM data. The dashed lines separate GRBs that are detected during

(below) or after (above) the prompt emission. Note that in some cases, including GRB 211211A, the Fermi/LAT observation started after the prompt phase, and we cannot exclude an emission starting before the detection time shown in the plot. **b**, LAT photon index versus LAT flux ($0.1\text{--}10\text{ GeV}$), both obtained through time-integrated analysis in ref. ²⁷.

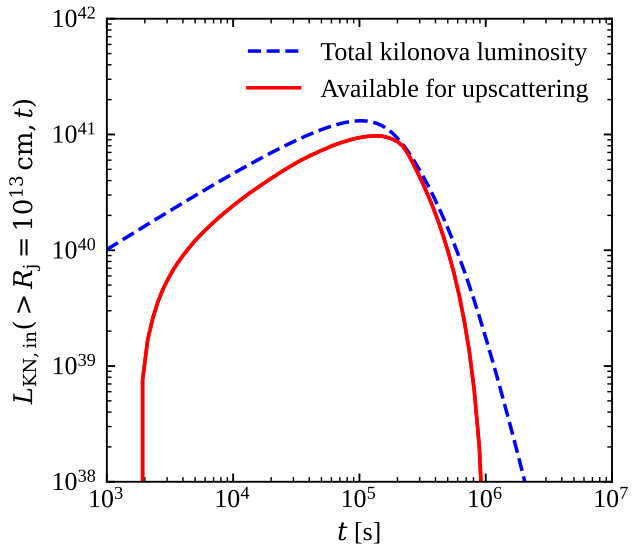


Extended Data Fig. 3 | Corner plot of the 12-dimensional posterior obtained from MCMC sampling. The meaning of the parameters is explained in the text. The histograms on the diagonal show the one-dimensional marginalized posterior probability density for each parameter, with the red line showing the best fit and the dashed lines bracketing 90% (or 95% in case of upper limits)

credible ranges. Contours in the remaining two-dimensional plots show the one-, two- and three-sigma equivalent bounds of the joint posteriors of parameter pairs, while dots show qualitatively the distribution of posterior samples outside the three-sigma boundaries. The red lines and dots show the position of the best fit.



(a)

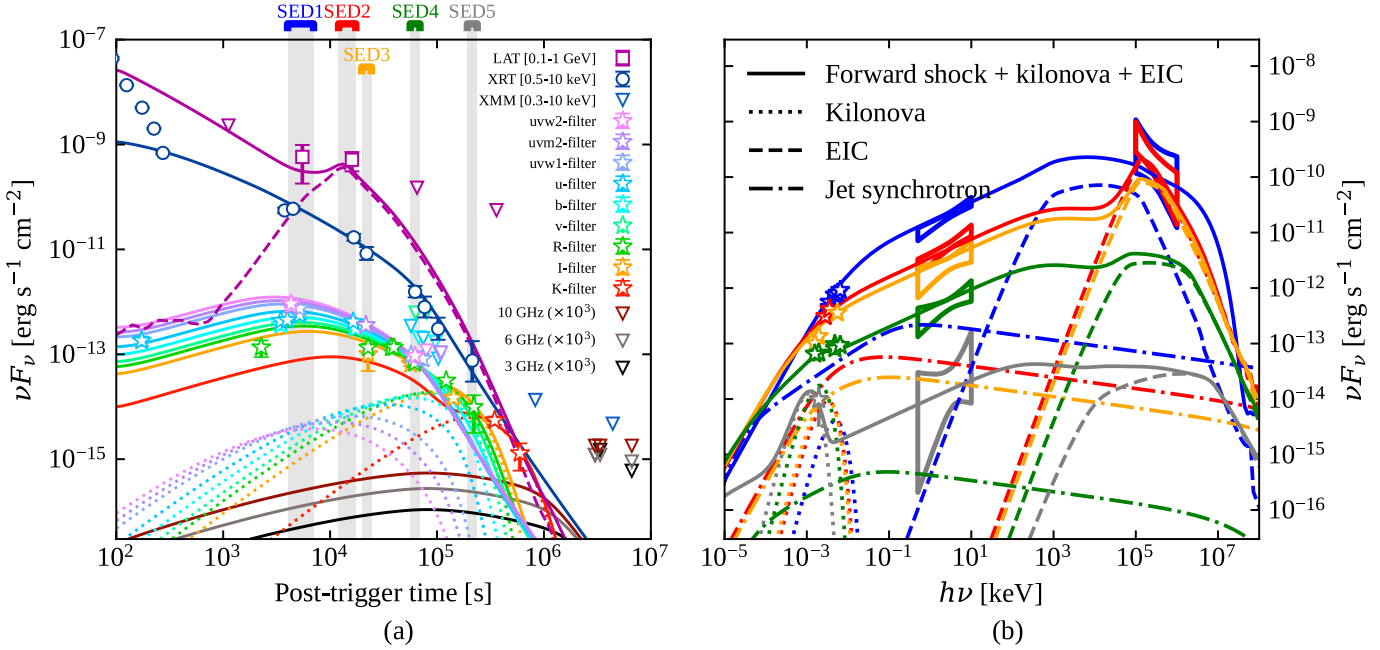


(b)

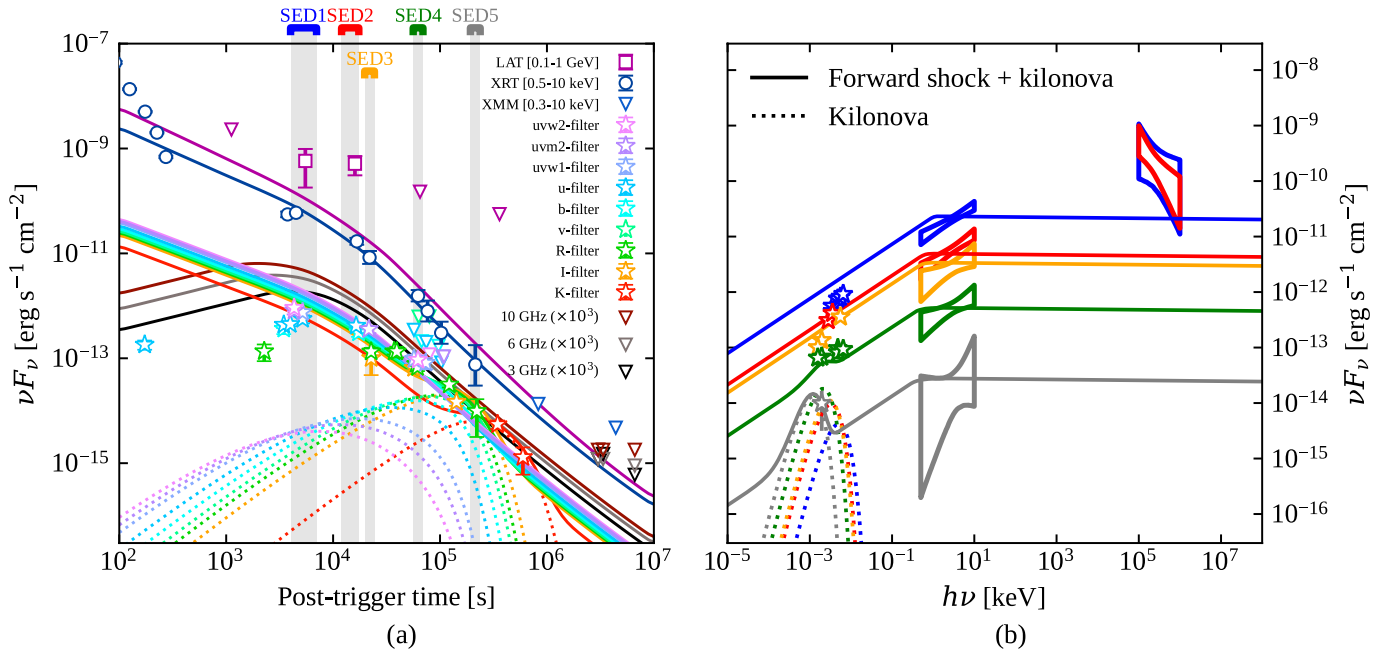
Extended Data Fig. 4 | Details on the kilonova photon transverse diffusion.

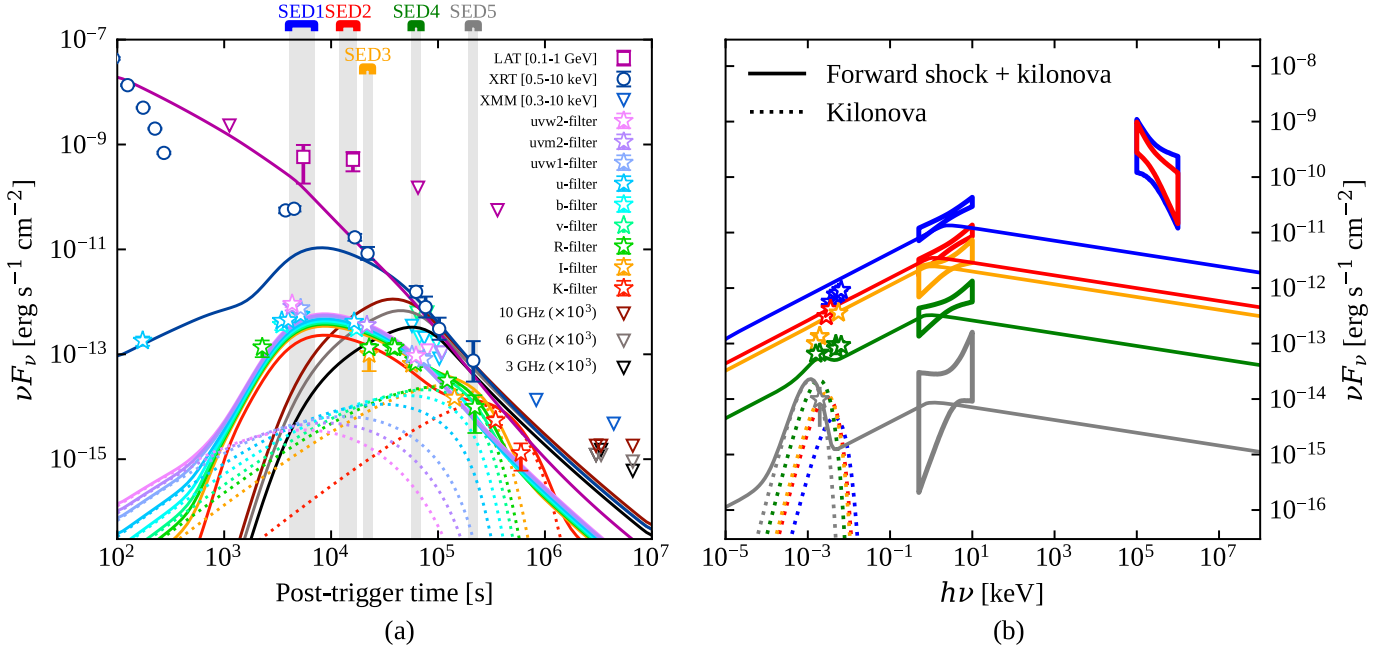
a, Kilonova luminosity that can diffuse from the jet-kilonova ‘walls’ above the jet dissipation region, located at R_j , at post-merger time $t = 10^4$ s. **b**, Kilonova

luminosity available for up-scattering within the jet dissipation region (red solid line), compared to the total kilonova luminosity (blue dashed line), assuming $R_j = 10^{13}$ cm.

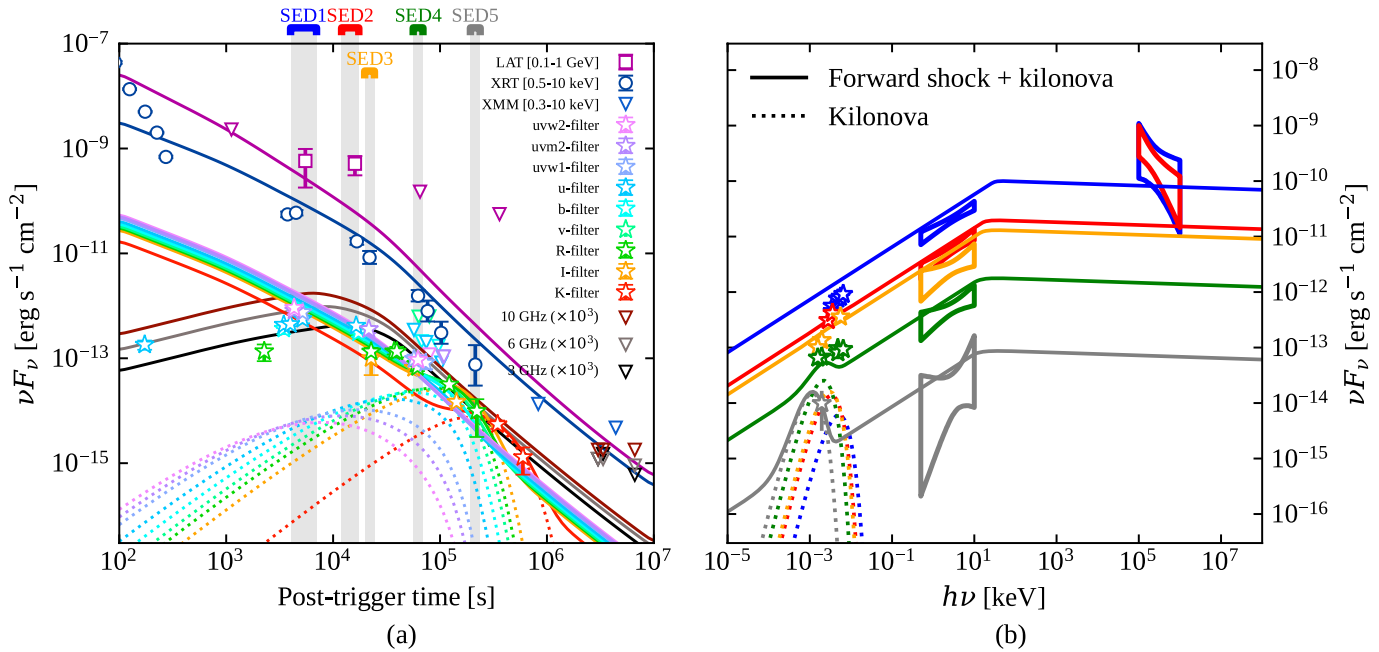


Extended Data Fig. 5 | Light curves as SEDs with models, showing the synchrotron emission from the low-power jet. **a, b**, Same as Fig. 3, but showing the model-predicted synchrotron emission from the low-power jet with dot-dashed lines in **b**.





Extended Data Fig. 7 | Comparison with the afterglow modelling in ref. 107. **a, b,** Light curves (**a**) and SEDs (**b**) with the best-fit parameters from ref. 107.



Extended Data Fig. 8 | Comparison with the afterglow modelling in ref.²⁶. **a, b,** Light curves (a) and SEDs (b) with the best-fit parameters from ref.²⁶.

Extended Data Table 1 | High-energy photons from GRB 211211A detected by Fermi/LAT

Energy (GeV)	Probability	Distance (deg.)	Arrival time (sec.)
0.21	0.94	0.36	6438.18
0.19	0.95	1.04	6647.43
0.16	0.93	1.34	12493.41
0.12	0.96	0.71	12612.52
1.74	0.97	0.32	12966.74
0.10	0.96	0.77	13053.43
0.12	0.92	1.69	13292.13
0.29	0.91	1.22	17860.45
0.23	0.97	0.67	18127.51

The energy of the photons, probability of association to the GRB, distance from the GRB location (as respect to RA=212.272°, DEC=27.884°) and the arrival time of the photons from the trigger time with probability more than 0.9.

Article

Extended Data Table 2 | Results of the forward shock + kilonova model fit

Parameter	Posterior ^a	Prior bounds
$\log(E/\text{erg})$	$53.2^{+0.8}_{-1.0}$	(50, 55)
$\log(n/\text{cm}^{-3})$	< -4.2	(−6, 2)
$\log(\Gamma_0)$	$3.1^{+0.9}_{-0.6}$	(1, 4)
$\log(\theta_j/\text{rad})$	$-1.74^{+0.18}_{-0.19}$	(−2, 0)
$\log \epsilon_e$	$-1.6^{+1.0}_{-0.67}$	(−3, −0.3)
$\log \epsilon_B$	$-2.5^{+1.1}_{-1.0}$	(−7, −0.3)
$\log \chi_e$	< -0.52	(−2, 0)
p	$2.31^{+0.14}_{-0.10}$	(2.01, 2.99)
$\log(m_{\text{ej}}/\text{M}_\odot)$	$-1.7^{+0.17}_{-0.17}$	(−4, 0)
$\log(\kappa/\text{cm}^2 \text{ g}^{-1})$	$-0.21^{+0.36}_{-0.31}$	(−1, 2)
$\log(v_{\text{max,ej}}/c)$	$-0.71^{+0.25}_{-0.24}$	(−2, −0.2)
$\log(f_{\text{sys}})$	$-0.77^{+0.20}_{-0.21}$	(−5, 0)

^a Best fit value (median of posterior samples) and 90% credible range (or 95% credible upper limit) constructed from marginalised posterior.

Parameters of our forward shock + kilonova model, summary results from our MCMC analysis, and bounds of the adopted priors. ^aBest-fit value (median of posterior samples) and 90% credible range (or 95% credible upper limit) constructed from marginalized posterior.